Variability of the infrared complex refractive index of African mineral dust: experimental estimation and implications for radiative transfer and satellite remote sensing

C. Di Biagio[1,*], H. Boucher[2], S. Caquineau[2], S. Chevaillier[1], J. Cuesta[1], and P. Formenti[1]

[1] LISA, UMR CNRS 7583, Université Paris Est Créteil et Université Paris Diderot, Institut Pierre Simon Laplace, Créteil, France

[2] IPSL/LOCEAN, UMR 7159-IRD-CNRS-UPMC-MNHN, Institut de Recherche pour le Développement, Bondy, France

Correspondence to: C. Di Biagio (claudia.dibiagio@lisa.u-pec.fr)

Abstract

Experimental estimations of the infrared refractive index of African mineral dust have been retrieved from laboratory measurements of particle transmission spectra in the wavelength range 2.5-25 μm. Five dust samples collected at Banizoumbou (Niger) and Tamanrasset (Algeria) during dust events originated from different Western Saharan and Sahelian areas have been investigated. The real (n) and imaginary (k) parts of the refractive index obtained for the different dust samples vary in the range 1.1-2.7 and 0.05-1.0, respectively, and are strongly sensitive to the mineralogical composition of the particles, especially in the 8-12 μm and 17-25 μm spectral intervals. Dust absorption is controlled mainly by clays (kaolinite, illite, smectite), and, to a lesser extent, by quartz and calcium-rich minerals (e.g., calcite, gypsum). Significant differences are obtained when comparing our results with existing experimental estimations available in the literature, and with the values of the OPAC (Optical Properties of Aerosols and Clouds) database. The different datasets appear comparable in magnitude, with our values of n and k falling within the range of variability of past studies. However, literature data fail in accurately reproducing the spectral signatures of main minerals, in particular clays, and they significantly overestimate the contribution of quartz. Furthermore, the real and the imaginary parts of the refractive index from some literature studies are found not to verify the Kramers-Kronig relations, thus being theoretically incorrect. The comparison between our results, from Western Africa, and literature data, from different locations in Europe, Africa, and the Caribbean, nonetheless, confirms the expected

large variability of the dust infrared refractive index. This highlights the necessity for an extended systematic investigation of dust properties at infrared wavelengths.

For the five analysed dust samples, aerosol intensive optical properties relevant to radiative transfer (mass extinction efficiency, k_{ext}, single scattering albedo, ω, and asymmetry factor, g), have been calculated, by using the Mie theory, based on the estimated refractive index and measured particle size distribution. The optical properties show a large sample-to-sample variability, with k_{ext}, ω, and g varying in the range 0.05-0.35, 0.25-1.0, and 0.05-0.75. This variability is expected to significantly impact satellite retrievals of atmospheric and surface parameters (e.g. from the Infrared Atmospheric Sounding Interferometer, IASI) and estimates of the dust radiative forcing.

1. Introduction

Mineral dust is one of the most abundant aerosol species in the atmosphere and strongly contributes to the total aerosol content (Textor et al., 2007; Huneeus et al., 2012). The arid and semi-arid regions of West Africa, i.e. the Sahara and the Sahel, account for more than 60% of the total annual dust emission, and are by far the most significant sources of mineral dust at the global scale (Prospero et al., 2002; Laurent et al., 2008; Ginoux et al., 2012). Once emitted, African dust is transported for thousands of kilometres across the Atlantic Ocean (e.g., Ben-Ami et al., 2009 and 2010) and the Mediterranean basin (e.g., Israelevich et al., 2002), thus affecting the environment at intercontinental distances.

Mineral dust directly affects the planetary radiative balance by absorption and scattering of radiation (Sokolik and Toon, 1996). Due to their high atmospheric load, dust aerosols are observed to exert a significant radiative effect both close to source regions and in transport areas (Haywood et al., 2003; Highwood et al., 2003; Di Biagio et al., 2010). As a consequence of the effect on radiation, mineral dust impacts the atmospheric thermal structure and stability (Kishcha et al., 2003; Heinold et al., 2008), with possible effects on cloud formation and properties (Rosenfeld et al., 2001; Klüser and Holzer-Popp, 2010), as well as on atmospheric photochemical reactions (Casasanta et al., 2011). The implications on the hydrological cycle, in particular, are of great relevance for water-stressed semi-arid areas, as it is the case of the Sahel, mainly in relation to possible feedback mechanisms on dust emission in these regions (Carlsaw et al., 2010).

Due to its characteristic mineralogical composition and extended particle size spectrum (from tenths of nanometers to tenths of micrometers), mineral dust effectively interacts with both the solar and the terrestrial infrared radiation fields (Ackerman and Chung, 1992; Hsu et al., 2000; Brindley and Russell, 2009). In terms of magnitude, the instantaneous solar effect is considerably larger than the infrared one, which generally becomes relevant only for very high dust amounts (e.g., Slingo et al., 2006). However, while the solar contribution is effective only during daytime, the infrared contribution acts throughout the 24-hours, thus on a daily basis it may compensate for a large fraction of the diurnal shortwave perturbation (e.g., di Sarra et al., 2011). The infrared contribution needs therefore to be taken into account in order to estimate the whole dust radiative effect.

The interaction of atmospheric dust with infrared radiation has also been shown to significantly affect the interpretation of remote sensing data. In particular, several key climate parameters, such as the atmospheric temperature profile, sea surface temperature, and greenhouse gases concentration, are derived from satellite measurements over narrowband infrared channels (MODIS, Moderate Resolution Imaging Spectroradiometer; SEVIRI, Spinning Enhanced Visible and Infrared Imager; AVHRR, Advanced Very High Resolution Radiometer; HIRS, High-resolution Infrared Radiation Sounder; AIRS, Atmospheric Infrared Sounder; and IASI, Infrared Atmospheric Sounding Interferometer). Misinterpretations of the data occur when the infrared radiative effect of dust is not accurately taken into account within satellite inversion algorithms (e.g., Ackerman, 1997; Sokolik, 2002; DeSouza-Machado et al., 2006). On the other hand, the dust infrared signature obtained in satellite data, especially in the 8-12 μm window region, is used to detect the presence and estimate the properties of dust from space (Legrand et al., 2001; Pierangelo et al., 2004; Klüser et al., 2011; Banks and Brindley, 2013; Capelle et al., 2013).

Still, very large uncertainties persist in the estimation of the dust infrared radiative effect (Haywood et al., 2005; Balkanski et al., 2007; Bierwirth et al., 2009). One of the main causes for this is the poor knowledge of the dust optical properties in this portion of the spectrum (e.g., Wang et al., 2006). Dust infrared optical properties cannot be directly measured by in situ instruments, and also their estimation based on ground-based or satellite remote sensing observations is difficult, due to the fact that the aerosol signature is partly covered by that of main atmospheric constituents (water vapour, CO_2) and that a priori knowledge of the investigated optical properties is often required by inversion algorithms. Thus, dust infrared optical properties are generally estimated through an alternative approach, which consists in

calculating them based on the knowledge of the physico-chemical properties of particles , i.e. composition, size distribution, and shape (Levin and Lindberg, 1979; Highwood et al., 2003).

In this sense, the complex refractive index, $m = n - ik$, the parameter linking the physico-chemical and the optical properties of aerosols, remains a major unknown (e.g., Sokolik et al., 1993; Claquin et al., 1998).

The complex refractive index of dust is mainly controlled by particle mineralogical composition (Patterson et al., 1981; Sokolik et al., 1998). Dust is composed of several minerals, such as clays (kaolinite, illite, smectite, chlorite), quartz, calcium-rich carbonates (calcite, dolomite) and sulphates (gypsum), feldspars (orthose, albite), and iron and titanium oxides, each characterised by specific lattice vibrational-rotational transitions, therefore by their own spectral refractive index in the infrared (Sokolik and Toon, 1999). Consequently, the magnitude and the spectral dependence of the complex refractive index of dust depend on the abundance and state of mixing (internal or external) of its main constituents (e.g., Mishchenko et al., 2004). Due to the diverse soil mineralogy of the different source areas (Claquin et al., 1999), the composition of dust aerosols varies depending on the region of origin (e.g., Caquineau et al., 2002). The proportion between the different minerals at emission also critically depends on the surface wind speed of erosion, which also determines their size distribution (Gomes and Gillette, 1993; Marticorena and Bergametti, 1995). Quartz, feldspars, and calcium-rich species are generally more abundant in the coarse mode component, while clays dominate the fine fraction (e.g., Pye et al., 1987; Kandler et al., 2009). The mineralogical composition of dust then changes rapidly after emission mainly as a consequence of the progressive loss of coarse particles due to gravitational settling (Schütz et al., 1981; Maring et al., 2003). This process reduces the abundance of quartz, feldspars, and calcium-rich species in the dust aerosol, thus yielding particles richer in clays. Also, when travelling over marine or polluted environments, the composition of dust may be additionally modified due to the interaction with other aerosol types (e.g., sea salts, soot) or atmospheric gases (e.g., nitrates, sulphates) (Formenti et al., 2011). As a consequence of all these processes, the complex refractive index of mineral dust is expected to vary as a function of the source region and during atmospheric transport. The complete characterization of this variability is necessary to evaluate the magnitude of the dust radiative effect along its whole atmospheric lifecycle.

A very few number of studies, from a limited number of geographical locations worldwide (e.g., Germany, Barbados, Niger), have investigated the complex refractive index of dust

aerosols at infrared wavelengths (Volz, 1972 and 1973; Fisher, 1976; Patterson, 1981; Fouquart et al., 1987; see also Sokolik et al. (1993) and (1998) and references therein). Hence, to date, the natural variability of the dust infrared refractive index is not represented. Moreover, some degree of uncertainties remains on the accuracy and representativeness of these few data. In all of these studies the refractive index of dust is estimated by means of the spectroscopy pellet technique. This approach consists in dispersing the aerosol particles in a matrix of transparent material, e.g. potassium bromide (KBr), which is then pressed to form a homogeneous pellet. A typical fraction of 0.1% of dust particles is dispersed in a total of 100-300 mg of KBr. The reflectance or transmission spectrum of the pellet is then measured and analysed by means of an appropriate optical theory to retrieve the complex refractive index of the particles. The pellet technique presents however several limitations which means it is not fully adapted to investigate aerosols. At first, this technique requires one to manipulate the aerosol sample, mixing it with KBr, and then to press the mixture to form the pellet. These operations may modify the physico-chemical properties of the particles, thus reducing the representativeness of the analysed samples compared to natural airborne conditions. In particular, the aerosol size distribution, as well as the morphology of the particles, may be affected by these modifications mainly due to the pressing during pellet production. Moreover, the fact of dispersing a very small quantity of aerosol (0.1%) in the KBr matrix determines a strong suppression of the aerosol scattering signal, which becomes almost negligible compared to that from the matrix itself. As a consequence, mainly the absorption component of the extinction is measured with the pellet technique, with a strong underestimation of the scattering fraction. This aspect is particularly important for dust particles, for which scattering is estimated to significantly contribute to the atmospheric infrared extinction (Dufresne et al., 2002). Despite these limitations and uncertainties, nonetheless, pellet spectroscopy data represent nowadays the only available references for dust infrared optical properties, and are used as the main basis for global aerosol databases such as OPAC (Optical Properties of Aerosols and Clouds; Hess et al., 1998) and GADS (Global Aerosol Data Set; Koepke et al., 1997).

In this study we apply the spectroscopy pellet technique to provide new experimental estimates of the infrared complex refractive index of dust aerosols. Natural particle samples from Western Sahara and the Sahel, some of the strongest sources at the global scale (Ginoux et al., 2012), have been considered. The paper has two main objectives: (i) to test the sensitivity of the dust infrared refractive index to the physico-chemical properties of the

particles, in particular to the mineralogy. We want to show that, also at the small scale (Western Africa), there is a significant variability of the dust refractive index as a function of particle properties that past studies are only in part able to detect; (ii) to show the importance of this variability on radiative forcing calculations and satellite remote sensing. The dust refractive index has been estimated in this study from spectroscopy pellet transmission measurements by applying an experimental procedure and a retrieval scheme mostly consistent with those of past literature studies (see also Sect. 2.1). We have made this choice, aware of the limitations and uncertainties of the spectroscopy technique discussed above, to simplify the comparison between past and new data, thus allowing an easier evaluation of the dust refractive index variability.

Dust samples analysed here have been collected during the AMMA 2006 campaign (African Monsoon Multidisciplinary Analysis; Redelsperger et al., 2006) at the ground-based super-sites of Banizoumbou (13.5°N, 2.6°E, 250 m above sea level), located in a remote area ~60 km east of Niamey in Niger (Rajot et al., 2008), and Tamanrasset (22.8°N, 5.5°E, 1370 m above sea level), in the heart of the Hoggar massif in South Algeria (Cuesta et al., 2008). Five different dust cases were selected based on their different origin and mineralogical composition, three from the Banizoumbou site (sample ID SOP0-47, SOP1-8, and SOP1-17), and two from Tamanrasset (sample ID N32 and N93). As here we want to focus on the refractive index variability near source regions, the five cases have been chosen to be representative of local emission episodes or of dust at most after 1-2 days of atmospheric transport. A summary of the main information for the selected Banizoumbou and Tamanrasset dust events is reported in Table 1. A more detailed discussion of the five dust episodes and identification of their different source regions is provided in Appendix A.

The paper is organised as follows: In Sect. 2 we present the measurements used in this analysis, the experimental method, and the main algorithm for complex refractive index estimation. The physico-chemical properties obtained for the considered samples are discussed in Sect. 3. Section 4 is then dedicated to the presentation and discussion of the spectroscopy measurements and complex refractive index results. The effect of the variability of the refractive index and size distribution on the optical properties of dust, as well as its possible implications on radiative transfer and satellite remote sensing, is investigated in Sect. 5. The main conclusions of this study are discussed in Sect. 6.

2. Measurements and methods

Dust aerosol samples have been collected at the two sites of Banizoumbou and Tamanrasset on 47-mm polycarbonate Nuclepore filters (nominal pore size 0.4 μm). The sampling time for the different cases (see Table 1) varied between a few hours to 1-2 days, depending on the aerosol concentration and the duration of the event. Dust particles deposited on filters have been analysed to obtain their bulk mineralogical composition. Then the infrared transmission spectra have been measured on the samples of collected dust to estimate their complex refractive index. The number size distribution of dust particles in the diameter range 0.3-20 μm was measured during filter sampling by means of a Grimm Optical Particle Counter (OPC, model 1.108). Full details on spectroscopy measurements and algorithm for complex refractive index estimation, dust filter chemical analyses, and procedures for size distribution data corrections are provided in the next paragraphs.

2.1 Infrared spectroscopy and dust complex refractive index estimation

Transmittance spectra (T) of collected dust particles have been recorded in the wavelength range 2.5–25 μm (4000-400 cm^{-1} wavenumber) at 2 cm^{-1} resolution by means of a Bruker Optics Equinox 55 FT-IR spectrometer. The instrument uses a Globar source, with a KBr beamsplitter and a deuterated triglycine sulphate (DTGS) detector. The infrared transmission spectroscopy has been performed by means of the usual pellet technique (i.e., Volz, 1972; Mooney and Knacke, 1985) using KBr as transparent matrix in which dust grains have been dispersed.

Dust particles collected on Nuclepore membranes need to be extracted from filters to mix with the KBr powder and then to produce the pellets. As discussed in the Introduction, the manipulation of dust particles is a delicate operation and it should be achieved by avoiding as much as possible contaminations or modifications of the sample. We tested different procedures to optimize dust extraction and KBr mixing. Our best obtained experimental protocol is described in the following: (i) *Suspension of dust particles in ethanol solution.* To allow dust particles to detach from the filter membranes, filters are immersed, dust-loaded face downward, in 10-15 ml of ethanol and shaken for ~5-10 minutes at ultrasonic frequencies. The ultrasonic shaking procedure is repeated 2-3 times, until the aerosol has completely detached from the filter; (ii) *Separation of dust and ethanol.* The dust-ethanol suspension is centrifuged at a speed of 11000 rpm for ~1 hour, thus permitting an effective

separation between the liquid (ethanol) and the solid (dust) phases. After centrifugation the dust-ethanol solution is left in vertical position for 1 day to sediment dust particles which had remained in suspension. At this point, having the liquid and solid phases well separated, ~95% of ethanol is removed by pipe aspiration, while the remaining ~5% is left to evaporate for 1 day; (iii) *Dilution of dust particles in the KBr matrix.* Once extracted and transferred to a glass tube, dust particles are weighed and then diluted in a KBr matrix. A high-quality pure potassium bromide (ACROS Organics IR grade) is used. The mass of KBr is set to obtain a total of 0.1% of dust in the mixture. Dust and KBr are weighed by means of a Sartorius microbalance (model LE225D) whose maximum sensitivity is 10 μg. The dust-KBr mixture is then mechanically shaken for about 10 minutes to create a homogeneous mixing. The obtained dust-KBr samples and the pure KBr are placed in the oven to dry at the temperature of 100 °C for ~12 hours. Putting the samples in the oven does not modify the dust mineralogical composition, as at these temperatures the main effect is water evaporation; (iv) *Pellet production.* Each of the 5 dust-KBr mixture samples is softly grounded in agate mortar, in order to slightly change the size of dust grains, and then is pressed under vacuum at the pressure of ~10 Tons cm^{-2} for 1-2 minutes to form a thin pellet. About 150 mg of powder is needed to create a homogeneous pellet of 13 mm diameter (surface 1.33 cm^2) and <1 mm thickness. Three pure 150 mg KBr pellets are also produced. Then all the pellets are put in the oven at 100 °C for about 1-2 hours until they are used for transmission spectroscopy measurements. This is done to avoid as much as possible water vapour absorption, in particular by the highly hygroscopic KBr. We should expect, as already mentioned, that some of the dust properties, such as the size distribution, aggregation state, or also the morphology of the particles, may partly change during the pellet production, thus affecting the representativeness of the analysed sample compared to airborne conditions. It should be pointed out, however, that the estimation of the effects of these modifications on the measured spectra is very difficult, and a certain degree of uncertainty on this aspect remains not quantified. All the laboratory operations we have described here are accomplished in clean conditions, i.e., working in a permanently ventilated room, and manipulating the samples in a laminar flow bench.

Spectroscopic measurements have been performed on the 5 dust-KBr and the 3 pure KBr samples. Pellets were placed in the spectrometer chamber purged of CO_2 gas and H_2O vapour. A total of 20 and 40 scans were averaged to produce the dust-KBr and the pure KBr spectra, respectively. The 3 spectra of pure KBr have been averaged and used to correct the

baseline of dust-KBr. This correction allows removing the signal due to the water vapour or other gases possibly absorbed on the pellet by KBr. Once corrected for the baseline signal, the dust-KBr spectra have been smoothed by performing a 9-point running average.

Starting from the measured dust-KBr transmission spectra, the real (n) and the imaginary (k) parts of the dust refractive index have been estimated following the procedure already applied by various authors to investigate Martian dust (Orofino et al., 1998; Marzo et al., 2004; Marra et al., 2005). The hypotheses at the base of our retrieval scheme, as will be discussed in the following, are consistent with the main assumptions made in most past studies on dust aerosols available in the literature (e.g., Volz 1972 and 1973; Fouquart et al., 1987).

Based on the Beer-Bouguer-Lambert law, the spectral transmittance, T(λ), through a thin section of a specific medium is given by:

$$\ln\left(\frac{1}{T(\lambda)}\right) = \alpha_{ext}(\lambda)\cdot x \quad (1)$$

where $\alpha_{ext}(\lambda)$ is the spectral extinction coefficient of the medium and x the pathlength of radiation. In our case the medium is a pellet composed of a matrix of transparent material (KBr) in which a small amount of grain particles (dust) are uniformly dispersed. $\alpha_{ext}(\lambda)$ may thus be written as the product of the grain extinction cross section, $C_{ext}(\lambda)$, by the *f*/V ratio, where *f* is the volume fraction of grain particles in the sample and V is the volume of a single particle (Bohren and Huffman, 1983). We can imagine grain particles to be compressed within the pellet in a homogeneous slab (*f*=1) of thickness $d = \frac{M}{\rho S}$, with M the total grain mass contained in the pellet, ρ the density of the grain material, and S the surface of the pellet, to obtain:

$$\alpha_{ext}(\lambda) = \frac{C_{ext}(\lambda)}{V} = \frac{3}{4}\frac{Q_{ext}(\lambda)}{a} \quad (2)$$

where $Q_{ext}(\lambda)$ is the grain extinction efficiency and *a* the particle radius. The dust density is set at 2.5 g cm^{-3} for all the samples. This value is chosen approximately at the mean of the range of desert dust densities as reported in the literature, i.e. 2.1-2.75 g cm^{-3} (i.e., Maring et al. 2000; Winfield, 2000; Iwasaka et al., 2003; Reid et al., 2003; Fratini et al., 2007).

In case extinction is dominated by absorption, $Q_{ext} \sim Q_{abs}$, as it can be assumed at infrared wavelengths for dust in pellets, we can write explicitly the $Q_{abs}(\lambda)/a$ ratio as a function of the measured transmittance as:

$$\frac{Q_{abs}(\lambda)}{a} = \frac{4}{3}\frac{\rho S}{M}\ln\left(\frac{1}{T(\lambda)}\right) \quad (3)$$

For very small grains ($a \ll \lambda$, i.e., the Rayleigh limit) embedded in a matrix of transparent material, the ratio between the absorption efficiency and the particle radius can be written following Mie theory for Rayleigh spherical particles as (Bohren and Huffmann, 1983):

$$\frac{Q_{abs}(\lambda)}{a} = \frac{8\pi}{\lambda}\sqrt{\varepsilon_m}\,\mathrm{Im}\left(\frac{\bar{\varepsilon}(\lambda)-1}{\bar{\varepsilon}(\lambda)+2}\right) \quad (4).$$

$\varepsilon_m = \left(n_{0,m}\right)^2$ is the real dielectric function of the matrix, with $n_{0,m}$ the real component of the KBr refractive index, and $\bar{\varepsilon}(\lambda)$ the dielectric function of the grain material relative to the matrix. The value of $n_{0,m}$ for KBr has been set at 1.54, constant in the infrared spectral range considered, as also reported in Orofino et al. (1998), and thus ε_m=2.37. The verification of the Rayleigh limit $a \ll \lambda$ has been tested for our dust samples using co-located measurements of the particle number size distribution (Grimm data shown in Fig. 1 and discussed in the next sections). At the wavelengths of 10 and 20 μm, the condition $a/\lambda < 0.1$, which can be considered satisfactory to verify the Rayleigh limit, is fulfilled on average by the 94 and 98% of particles (in number), respectively. Moreover, in our formulation (Eq. (4)) we assume dust particles to have a spherical shape, and thus to be described by the Mie theory. Taking into account particle non-sphericity would require a much more complex retrieval scheme. We have decided to neglect this effect at this stage, thus maintaining retrieval conditions which are similar to those of previous literature studies on the dust refractive index.

The dielectric function in Eq. (4) may be written using the Clausius-Mossotti relation as the sum of N Lorentzian harmonic oscillators:

$$\frac{\bar{\varepsilon}(\omega)-1}{\bar{\varepsilon}(\omega)+2} = \frac{\bar{\varepsilon}_v(\omega)-1}{\bar{\varepsilon}_v(\omega)+2} + \left[\sum_{j=1}^{N}\frac{F_j}{\omega_j^2-\omega^2-i\gamma_j\omega}\right] \quad (5)$$

where ω is the angular frequency of radiation ($\omega = 2\pi c/\lambda$, [s^{-1}]), c is the velocity of light in vacuum, and $\bar{\varepsilon}_v$ is the real dielectric function of the grain material relative to the matrix in the

limit of high frequencies, i.e., at visible wavelengths, $\bar{\varepsilon}_v = \left(\frac{\varepsilon_g}{\varepsilon_m}\right)_{vis}$ with $\varepsilon_g = \left(n_{0,g}\right)^2_{vis}$ and $\varepsilon_m = \left(n_{0,m}\right)^2_{vis}$, square of the real components of the refractive index at visible wavelengths for the grain material and the matrix, respectively. $\left(n_{0,m}\right)_{vis}$ and $\left(n_{0,g}\right)_{vis}$ have been set at 1.57 and 1.53, respectively, as the mean of the values reported in literature for KBr (e.g. Orofino et al., 1998) and African dust (Osborne et al., 2008; Petzold et al., 2009; McConnell et al., 2010; Klaver et al., 2011). Our choice of $\left(n_{0,g}\right)_{vis}$=1.53 is also in agreement with the values reported by most of past literature studies on the dust infrared refractive index (see data shown in Fig. 7). (ω_j, γ_j, F_j) are the three fundamental parameters characterizing the j-th oscillator, and in particular ω_j is the eigenfrequency, γ_j is the damping factor, and F_j is a quantity related to the plasma frequency strength, $\omega_{p,j}$, and the oscillator strength, f_j, through the relation $F_j = \frac{1}{3} f_j \omega_{p,j}^2$. By combining Eq. (4) and (5), we have:

$$\frac{Q_{abs}(\omega)}{a} = \frac{4\omega}{c}\sqrt{\varepsilon_m}\left[\sum_{j=1}^{N}\frac{F_j\gamma_j\omega}{\left(\omega_j^2-\omega^2\right)^2+\gamma_j^2\omega^2}\right] \quad (6)$$

Starting from the transmission measurements and by applying Eq. (3) an experimental estimation of the ratio $Q_{abs}(\omega)/a$ can be obtained. A non-linear fit procedure is then applied to the experimental $Q_{abs}(\omega)/a$ spectrum to determine the 3N values of the oscillator parameters (ω_j, γ_j, F_j) in Eq. (6). Once estimated, the 3N parameters are used to calculate the dielectric function of the grain material relative to the matrix, $\bar{\varepsilon}(\lambda)$, by applying Eq. (5). The absolute dielectric function of the grain material $\varepsilon_g(\lambda) = \varepsilon_g^{'} - i\varepsilon_g^{''}$ is then estimated by multiplying $\bar{\varepsilon}(\lambda)$ by ε_m. Finally, the spectral real, $n_g(\lambda)$, and imaginary, $k_g(\lambda)$, parts of the grain material complex refractive index can be determined using the following equations:

$$n_g = \left(\frac{1}{2}\left[\sqrt{\left(\varepsilon_g^{'}\right)^2+\left(\varepsilon_g^{''}\right)^2}+\varepsilon_g^{'}\right]\right)^{1/2} \qquad k_g = \left(\frac{1}{2}\left[\sqrt{\left(\varepsilon_g^{'}\right)^2+\left(\varepsilon_g^{''}\right)^2}-\varepsilon_g^{'}\right]\right)^{1/2} \quad (7)$$

The real and imaginary parts of both the dielectric function and refractive index are not independent quantities. They are related through the Kramers-Kronig relations, which for the refractive index can be written as:

$$n_g(\omega) - 1 = \frac{2}{\pi} P\int_0^{\infty} \frac{\Omega \cdot k(\Omega)}{\Omega^2 - \omega^2} \cdot d\Omega \qquad k_g(\omega) = -\frac{2\omega}{\pi} P\int_0^{\infty} \frac{n(\Omega)}{\Omega^2 - \omega^2} \cdot d\Omega \qquad (8)$$

where P is the Cauchy Principal value of the integral. It should be noticed that the retrieval method based on the Lorentzian dispersion theory used here allows to obtain $\left(\varepsilon_g^{'}, \varepsilon_g^{''}\right)$ and (n_g, k_g) couples which automatically satisfy the Kramers-Kronig relations.

2.2 Dust mineralogical composition

Different techniques have been combined to yield the most complete characterization of the composition of mineral dust, including: (i) Wavelength Dispersive X-Ray Fluorescence (WD-XRF, Panalytical PW-2404 spectrometer) to determine the dust elemental composition (Na, Mg, Al, Si, P, K, Ca, Ti, Fe); (ii) X-Ray Diffraction (XRD, Siemens D500 diffractometer) to estimate the particles' mineralogical composition in terms of clays (kaolinite, illite, smectite, chlorite), quartz, calcium-rich species (calcite, dolomite, gypsum), and feldspars (orthose, albite); (iii) the citrate-bicarbonate-dithionite-method (CBD, Lafon et al., 2004) to determine the dust iron oxide content; (iv) the X-ray Absorption Near Edge Structure (XANES) and Extended X-ray Absorption Fine Structure (EXAFS) to retrieve the iron speciation between hematite and goethite. The details of the experimental protocols and data treatment for the different techniques are extensively discussed in Caquineau et al. (1997 and 2002), Lafon et al. (2004), Klaver et al. (2011), and Formenti et al. (2008; 2014). The full set of analyses mentioned above has been carried out on the SOP0-47, SOP1-8, and SOP1-17 Banizoumbou samples. Instead, for the N32 and N93 Tamanrasset samples only XRD measurements have been possible.

Starting from these measurements, the dust mineralogical composition for the different samples has been estimated through the procedure described in Appendix B.

2.3 Dust particle size distributions

The particle number size distribution between 0.3 and 20 μm on 15 size channels was measured at the two sampling sites by means of a Grimm OPC (Grimm Inc., model 1.108) (Heim et al., 2008) operated at 1-min (Tamanrasset) and 5-min (Banizoumbou) time resolution. The Grimm OPC was factory calibrated with monodisperse polystyrene sphere latex (PSL) whose complex refractive index at the instrument operating wavelength (780 nm)

is 1.59-0i. We have corrected the measured sphere-equivalent optical diameter in a sphere-equivalent geometrical diameter by taking into account the complex refractive index of the sampled aerosol (Liu and Daum, 2000). The optical-to-geometric diameter conversion has been done by recalculating the calibration curve considering the refractive index of dust aerosol. Optical calculations have been performed using Mie theory for spherical particles. The complex refractive index was set at 1.53-0.002i, within the range of values available in the literature for Saharan dust (e.g., Osborne et al., 2008; Petzold et al., 2009). After refractive index correction the diameter measurements range for the Grimm 1.108 became 0.38-28.9 μm.

The average of the size distribution data measured corresponding to each of the five dust filter samplings has been calculated. Continuous Grimm data were available for the three Banizoumbou SOPs dust events, whereas Tamanrasset measurements were acquired only at the end of the dust episode for N32 (26 July 2006 from 10:00 to 14:17) and at the beginning for N93 (5 October 2006 between 01:00 and 8:07).

3. Physico-chemical properties of the selected dust cases

Figure 1 shows the normalised number and volume size distributions obtained for the five different dust events considered in this study. All size distributions are characterised by a multimodal structure with five main modes, centred at about <0.6, 1, 2.5, 5, and 12 μm diameters. Because of the lower size cut of the Grimm OPC at 0.3 μm, the lower tail of the first mode at diameter <0.6 μm is not very well defined. N32 and N93 distributions show also an additional defined mode, centred at ~25 μm, not present in the SOPs cases. This additional mode is possibly associated to the resuspension of particles very locally at the Tamanrasset site during the dust events. In terms of number distributions, the samples show a similar particle content in the whole size range, with the exception of SOP1-8, which is richer in coarse particles (diameter >5 μm), and N93, which presents a lower particle content in the whole diameter range ~0.8-25 μm. For N93, this is likely due to the fact that Grimm has measured at the very early stage of the dust event, thus before the maximum of the atmospheric dust load. In order to model the behaviour of the size distribution data, multimodal lognormal fits have been performed, and the fitting curves obtained are also shown in Fig. 1. Seven lognormal modes have been necessary to fit the experimental curves. The mean of the 5 lognormal fitting curves obtained considering (mean_A) or discarding

(mean_B) the N32 and N93 mode at 25 μm has been calculated, and data are also plotted in Fig.1.

The mineralogical composition obtained for the five dust samples is reported in Table 2 and summarized as follows: (i) SOP0-47 and N32 are originated in the same source areas in North - Northwestern Niger, so they are characterized by the same mineralogical composition with ~89-90% of clays, 6% of quartz, and 4% of iron oxides. The only significant difference between the two is the clays partitioning, with only kaolinite and illite detected in SOP0-47, and also smectite identified as a major clay component in N32; (ii) even if sampled during a Sahelian erosion event, SOP1-17 presents a mineralogy very similar to that of SOP0-47 and N32. This may be explained considering that SOP1-17 particles has been collected more than 3 hours after the main erosion event had occurred, so likely after the dust plume has been deprived of its component of larger particles, rich in quartz and feldspars, due to the rapid gravitational settling process (Pye, 1987). This is also consistent with the size distribution measured for this sample. For SOP1-17, the only case for which iron speciation is available, goethite is observed to dominate over hematite (80% vs 20% of the iron oxide content); (iii) SOP1-8, sampled in correspondence of a strong Sahelian local erosion event, differs from all the other samples because of its low amount of clays (52%), mainly kaolinite and illite, and enrichment in quartz (40%) and feldspars (3%). The high quartz content also explains the larger fraction of particles, especially of diameter larger than ~10 μm, which account for ~60% of the particle volume size distribution, observed for this sample; (iii) N93 is characterized by a lower content of clays (67%), mainly kaolinite and smectite, together with larger amounts of quartz (17%) and calcium-rich species (11% of calcite and gypsum), the latter in particular indicative of Northwestern Sahara source areas.

4. Results

4.1 Dust infrared absorption spectra

The absorbance spectra ($A = \log_{10}(1/T)$, with T the transmittance) measured in the spectral range 2.5-25 μm for the five different dust samples are shown in Fig. 2. The uncertainty in the measured spectra is less than 3% and has been estimated as the 3σ variability of the signal in the regions of no dust absorption ($A<0.01$). This uncertainty takes account of the variability of the noise and the offset components of the measured signal.

The main features of the different spectra follow the signatures of clay species (kaolinite, illite, smectite; see Fig. 3 as a reference for single mineral features and Table 3 for identified band positions and their assignments). The dust largest absorption is observed in the window region 8-12 μm (maximum of A from 0.08 to 0.21) and at wavelengths larger than ~17 μm (maximum of A from 0.04 to 0.10), therefore where the strongest absorption bands of clays are found. Coincident or superimposing bands for the different clay species are present at ~9.0, 9.7, 9.9, 18.8, 19.3, 21.4, and 23.1 μm (band peak wavelengths), while an additional single band mainly associated to kaolinite is identified in the 10.4-11.2 μm spectral region. Absorption by quartz in the atmospheric 8-12 μm window region (single band at ~9.2 μm) and above 17 μm (two bands centred at ~20 and 22 μm) appears to be masked by the clay signals, while a more clear signature emerges at ~12-13 μm. This is the case for the quartz-rich SOP1-8 sample which shows an enhanced absorption over this band compared to the other dust cases. The calculated ratio of the quartz band peak intensity (at ~12.5 μm) between SOP1-8 and the other samples varies between a minimum of 1.32-1.36 for SOP1-17 and N93 to a maximum of 1.45-1.56 for SOP0-47 and N32, thus indicating the quartz in SOP1-8 to contribute by about 30-50% to the increase in absorption in this band.

As for the quartz, the spectral signatures of the other minerals, e.g. calcium-rich species, are apparent only when the absorption of clays becomes very low. This is the case of sample N93 for which it is possible to detect the signal of calcite at ~7 and ~11.4 μm, and also of gypsum, whose band between 8.2 and 9.2 μm appears to combine with the clays and quartz bands determining a broadening of the N93 spectrum in this part of the window spectrum. A small signature is also observed for all the different samples between 14 and 16 μm, possibly associated to the combined effect of calcium-rich minerals and iron oxides absorbing in this spectral interval (calcite, gypsum, hematite, goethite). Strongest signatures of iron oxides, which mainly occur at wavelengths larger than 15 μm (two large bands centred at ~19 and 23 μm for hematite, and one at ~18 μm for goethite), are instead very difficult to detect due to their superposition with clay bands.

Almost negligible differences in terms of the position of the absorption bands are observed for the different samples. Conversely, a marked sample-to-sample variability of the amplitude of the band peaks is noticed. In general, the lowest absorbance is observed for SOP1-8 while highest values are obtained for N32 and N93. This is likely linked to the clay content and its speciation, as well as dust size distribution, for the different dust cases. The weaker absorption observed for SOP1-8, for instance, can be associated to the lowest illite and

kaolinite content measured for this sample, thus reducing the clay minerals absorption features. The largest absorption of N32 and N93 may be instead related, at least as a first assumption, to the presence of smectite as a dominant clay species together with kaolinite. Major absorption bands of smectite are coincident and comparable or even stronger in intensity to those of kaolinite, so the combined effect of the two clays results in an enhancement of the absorption at these wavelengths. There is also another consideration to possibly explain the larger absorption obtained for the N32 and N93 samples. As already pointed out in Sect. 3, the two Tamanrasset samples present in their size distribution a defined mode of larger particles, more efficient in interacting with infrared radiation, compared to the Banizoumbou samples. This means that, even with a similar mineralogical composition of dust between the two sites, we have to expect larger absorption for Tamanrasset dust due to the differences in the size distribution. This assumption can be tested, for instance, by considering the peak value of kaolinite band at ~10.9 μm, for which we obtain slightly larger intensities for N32 and N93 samples (0.046 and 0.05, respectively) compared to those of the SOPs samples (0.043 for SOP0-47 and 0.033 for SOP1-8 and SOP1-17), which we know to have a similar or rather larger content of kaolinite. The role of the size distribution possibly allows also to explain the fact that sample N93, which has a global smaller content of clays but a larger fraction of coarse particles, presents an absorption which in intensity is comparable to that of the clay richer N32. The fact of observing differences in the absorption spectra which are coherent with the variability of the size distribution measured for the different samples indicates that the main features of dust size have changed little during sample manipulations and pellet production.

A few narrow peaks are also observed at ~2.7 μm for all the samples, at ~4.2 for SOP0-47 and SOP1-17, and at ~7.2 μm for SOP0-47, SOP1-8, and SOP1-17. The peaks at 4.2 and 7.2 μm are very likely due to CO_2 and organic matter, respectively, which have contaminated the samples after dust-KBr pellet production. The intensity of these narrow peaks appears to be proportional to the absorption band of H_2O observed between ~2.7 and 4 μm for all the samples (not shown in the spectra of Fig. 2 because it is removed through baseline correction), which in turn is associated to the KBr water absorption that occurred during spectroscopic manipulations. Absorption by carbonate species (i.e., calcite) may also partly contribute to the 7.2 μm band. The signal measured at 2.7 μm is instead mainly related to clays (kaolinite and illite) (Saikia and Parthasarathy, 2010). These narrow peaks have been taken into account in successive analyses.

4.2 Dust infrared complex refractive index

Starting from the measured transmittance spectra, the $Q_{abs}(\lambda)/a$ ratio has been calculated by applying Eq. (3). The uncertainty on the calculated $Q_{abs}(\lambda)/a$, taking into account the uncertainties on the measured spectra (<3%) and the estimated pellet dust content (<7%), varies between a minimum of 2.4% for N32 to a maximum of 6.4% for SOP1-8. As discussed in Sect. 2.1, a non-linear fit procedure has been applied to the experimental $Q_{abs}(\lambda)/a$ to obtain the values of the 3N parameters necessary to estimate the real and imaginary parts of the dust refractive index. The fitting procedure has been performed using the Levenberg-Marquardt technique (e.g., Pujol, 2007). Reasonable guesses for the oscillator parameters are manually entered as inputs, then the fitting routine returns optimized parameters. The initial number and position of oscillators is set to be equal to that of the absorption bands present in the experimental $Q_{abs}(\lambda)/a$ spectrum. Additional oscillators may be subsequently added in order to improve the results of the best fit procedure. To guarantee a successful analysis, however, the number of fitting oscillators should remain limited; furthermore, the obtained 3N oscillator parameters must all have positive values (Spitzer and Kleinman, 1961; Roush et al., 1991). The experimental $Q_{abs}(\lambda)/a$ spectra together with the theoretical curves obtained from the nonlinear fitting procedure are shown in Fig. 4. The number of oscillators used for each fit, also reported in the plot, is between 22 and 29. Residuals (R) between the experimental and the fitted $Q_{abs}(\lambda)/a$ and normalized by the measurement error have been calculated to verify the goodness of the results. An example is shown in Fig. 5, where the spectral R obtained for two of the five analysed dust samples (SOP1-8 and N93) are plotted. It indicates that the $Q_{abs}(\lambda)/a$ spectra are fitted within their estimated uncertainty ($|R|\leq 1$) approximately in the entire wavelength range with significant absorbance ($A>0.01$). Discrepancies between the experimental and the fitted curves ($|R|\leq 10$) are obtained for $\lambda<6$-7 μm and in a few narrow bands between 12 and 17 μm, thereby in spectral regions where dust absorption is close to zero. The set of 3N parameters estimated from the $Q_{abs}(\lambda)/a$ fits have been used to calculate, by applying Eqs. (5) and (7), the real and the imaginary parts of the refractive index.

A sensitivity analysis was carried out in order to assign an uncertainty to the retrieved values of n and k, whose determination is based on a minimization procedure. The sensitivity analysis is aimed at assessing how the uncertainties on the measured $Q_{abs}(\lambda)/a$ affect the retrieved parameters. To this purpose, the values of n and k are also obtained by using as

input the observed $Q_{abs}(\lambda)/a$ plus or minus one standard deviation on their measurement. The deviations of the values of n and k retrieved in the sensitivity study with respect to those obtained in the first inversion are assumed to correspond to the one standard deviation uncertainty. The results show the uncertainty is small (<1.5%, averaged over the whole spectral range) for the real part of the refractive index, while more significant (<25%) for the imaginary part. Another source of uncertainty for n and k, which we do not quantify in this study, is also associated to the choice of the $\left(n_{0,m}\right)_{vis}$ value in Eqs.(5)-(7), here set at 1.53 in agreement with past literature studies (Volz, 1973; Carlson and Benjamin, 1980; Longtin et al., 1988).

The real and the imaginary parts of the refractive index obtained for the five dust samples considered in this study are shown in Fig. 6. As expected, the retrieved n and k reproduce well the features detected in the absorbance spectra, both in terms of spectral signature and relative intensities between the different samples. Evident is the contribution of clays, especially in the 8-12 μm and 17-25 μm spectral intervals where multiple bands, reproducing the absorption due to kaolinite, illite, and smectite, are observed. The sharp transition from low absorption outside these spectral ranges to the maximum absorption within them, determines the largest variations of the refractive index. In the 8-12 μm window, the imaginary part rapidly increases from ≤0.001 to peak values of 0.3- 0.85, while the real part ranges between 1.1 and 2.0. Above 17 μm, k peaks at 0.45-1.0, and n varies between 1.2 and 2.7. As for the absorbance, refractive index data display a very weak quartz signature, with the only exception of the 12-13 μm band, where the absorption of quartz induces an increase of k to values of ~0.09 for SOP1-8 and <0.06 for the other samples. The contribution of calcite to the refractive index of N93 is marked at ~7 μm (k~0.07), while it is almost indistinguishable at ~11.4 μm. Also, a refractive index comparable to that of quartz and calcite (k~0.06-0.08) is observed at 14-16 μm due to the combination of calcite, gypsum, and iron oxides signatures.

A small red shift of less than 0.3 μm (or 10 cm^{-1}) is observed in correspondence of the different refractive index peaks compared to the experimental absorption spectra. This is possibly associated to the fact of using Mie theory to reproduce dust absorption in our retrieval algorithm. Our 10 cm^{-1} shift is however small compared to the 25-40 cm^{-1} Mie induced shift reported by several authors investigating the extinction spectra of several clay and non-clay dust constituent minerals (Hudson et al., 2008a and 2008b; Laskina et al. 2012).

559 This suggests the effect of shifting due to the use of Mie theory is partly mitigated when
560 considering the extinction spectra of dust particles instead of single minerals.

561 Our results show the dust refractive index to significantly vary in magnitude for the five
562 analysed samples. For instance, within the main clay absorption bands we obtain for N32 and
563 N93 values of k which are 2-3 times larger compared to SOP1-8. Differences up to 30-40%
564 are also observed for the real part in the cases considered. As discussed in Sect. 4.1, this
565 variability is linked to the variability of mineralogical composition and size distribution
566 observed for the different dust events. In conclusion, these results, despite obtained
567 considering aerosols from a limited number of sources from Western Africa, appear rather
568 significant as they clearly put in evidence the large sensitivity of the refractive index to the
569 physico-chemical properties of dust particles.

570

571 **4.3 Comparison with literature data and the OPAC database**

572 The results of our analysis have been compared with other studies providing direct estimates
573 (pellet spectroscopy data on dust collected at different sites, i.e. Germany, Barbados, Niger;
574 Volz, 1972, and 1973; Fouquart et al., 1987), and mineralogy-based calculations (Longtin et
575 al., 1988) of the dust infrared refractive index, as well as syntheses of available literature data
576 (Carlson and Benjamin, 1980; Sokolik et al., 1993). These studies have been selected as they
577 serve as the main basis for models for aerosol optical properties (e.g., Toon and Pollack,
578 1976; Shettle and Fenn, 1976 and 1979; WMO, 1986; D'Almeida, 1991) and global aerosol
579 databases, such as OPAC and GADS, all extensively used in a wide variety of radiative and
580 climatological studies. Besides, the OPAC aerosol database plays a very important role in
581 satellite remote sensing as it is the most used reference for dust properties in the retrieval
582 algorithms of several sensors measuring in the thermal infrared (MODIS, SEVIRI, AVHRR,
583 HIRS, AIRS, IASI) (see Table 1 in Klüser et al., 2012). Owing to its widespread utilisation
584 and relevance for atmospheric application, the complex refractive index of the desert aerosol
585 model from the OPAC database is also considered for comparison with our results.

586 The results of the comparison are shown in Fig.7. For both the real and the imaginary parts,
587 our estimates of the dust refractive index fall, over the whole considered spectrum, within the
588 range of variability reported in literature data. For the imaginary part, a similar spectral
589 behaviour is observed in the 8-12 μm window region between our data and the different
590 literature curves, with the only exception of Longtin et al. (1988) due to the large contribution

591 of quartz in their calculations. The spectral signatures from the different clay species appear
592 smoothed in the curves taken from literature, mainly because of the rather coarse spectral
593 resolution of these datasets. Only a major single peak between 9 and 10 μm is observed,
594 compared to our data where multiple clay peaks are detected in the 8-12 μm spectral interval.
595 The majority of the different datasets presents the signature of calcite at ~7 μm in the k
596 spectrum, as also observed in our data for the N93 sample. Above 11-12 μm, the imaginary
597 part of the refractive index obtained in this study is lower in magnitude compared to most of
598 literature data at nearly all spectral bands. For the real part of the refractive index, a
599 comparable spectral variability is obtained between our data and the different literature
600 datasets in the 2.5-17 μm spectral range, and a significant weaker variation is observed for
601 our results in the 8-12 μm window. The best agreement, also in terms of measured intensity,
602 is found with the real part from Volz (1972) in the whole 8-25 μm interval. For literature
603 data, and Longtin et al. (1988) in particular, a stronger contribution of quartz is observed in
604 both the real and the imaginary spectra, with strong peaks detected at ~9.2, 12.5, 20 and 22
605 μm. Furthermore, above 17 μm the different datasets, with the only exception of Fouquart et
606 al. (1987) and in part Volz (1973), appear to mostly not capture the signatures of clays, which
607 instead are observed to dominate our n and k experimental curves.

608 For both the real and the imaginary parts, the ensemble of literature data and our estimates
609 are observed to span a relative large interval of values. This variability is related, as a first
610 hypothesis, to the fact that the different studies refer to dust from diverse source regions as
611 well as to different stages of their atmospheric lifetime, thus to particles characterized by a
612 different composition and size distribution, and thus having different optical properties. A
613 large variability of the dust infrared refractive index has been also documented by Patterson
614 et al. (1981) and Otto et al. (2007), who compiled literature data from additional studies. For
615 instance, for the imaginary part they reported a range of values spanning the interval 0.02-1.0
616 at 8-12 μm, comparable to that in Fig. 8. Thus, the comparison between our results and
617 literature data confirms the large variability of the dust infrared complex refractive index as a
618 function of the physico-chemical properties of the particles.

619 As discussed by Sokolik et al. (1993), however, differences between the various datasets
620 might be associated not only to the specific physico-chemical state of the particles, but also to
621 uncertainties due to the different methods used to estimate the dust refractive index. This is,
622 for instance, the case when comparing our data with those by Volz (1972, 1973). In these
623 studies the real and imaginary parts of the dust refractive index were derived by two different

methods: the imaginary part using transmission measurements and the real part using reflectance measurements, both with the standard pellet technique. For the imaginary part, the transmission spectra inversion was performed by applying a method which is mostly consistent with our approach, as discussed in Sect. 2.1, and this also explains the good comparison with our data for k. For the real part they inverted the reflectance spectra by combining the specular reflectance law and the previous estimated imaginary part of the refractive index. We found, however, that by following this procedure they obtained real and imaginary parts of the refractive index which do not verify the Kramers-Kronig relationship, and this explains why there is a larger disagreement with our results for n, especially in the 8-12 μm window. Similar considerations are valid also for Carlson and Benjamin (1980) and OPAC data. This also implies that caution has to be used when making use of these refractive index data as, from a theoretical point of view, they are incorrect.

5. Infrared intensive optical properties of mineral dust: variability and implications

5.1 Sensitivity to refractive index and size distribution

Intensive optical properties relevant to radiative transfer (mass extinction efficiency, k_{ext}, m^2 g^{-1}; single scattering albedo, ω; asymmetry factor, g), have been calculated for the five analysed dust samples based on their estimated complex refractive index and measured particle size distribution.

Two sets of k_{ext}, ω, and g have been computed: (i) at first, calculations have been performed by considering for the different samples their own complex refractive index, while fixing a unique size distribution for all the cases (i.e., the mean_B average size distribution shown in Fig.1). This permits to focus exclusively on the effect of refractive index variability on the estimated properties; (ii) as a second approach, the own size distribution for each of the different samples has been used together with the complex refractive index to calculate k_{ext}, ω, and g. In this case, the combined effect of refractive index and size distribution variability will emerge from the results. In this study, we have decided to neglect the effect of particle shape (Kalashnikova and Sokolik, 2002; Nousiainen, 2009), and dust optical calculations have been performed using Mie theory for spherical particles. The ensemble of calculated dust optical properties is reported in Fig. 8. By comparison, the spectral optical properties obtained using the OPAC refractive index, calculated considering the mean_B size distribution, are also shown in the plot.

We consider at first data obtained for the fixed dust size distribution (Fig. 8a). Calculated optical properties, k_{ext} and ω in particular, follow the spectral signature and variability of the complex refractive index, with the strongest absorption observed in the window region and at wavelengths >17 μm. k_{ext} and ω vary within the range ~0.05-0.25 m^2 g^{-1} and ~0.25-1.0, respectively. The asymmetry factor is observed to decrease approximately linearly with λ for all the samples, with values ranging from a maximum of ~0.75 at 2.5 μm to a minimum of 0.25 at 25 μm. Moderate differences are obtained between the different samples for k_{ext} and g, while larger variations are observed for ω, especially below 10 μm and within the range 12-23 μm. In comparison to our data, the calculation based on the OPAC refractive index appears to overestimate dust extinction (up to 0.1 m^2 g^{-1} increase), especially at 9-10 μm, mainly due to the stronger contribution of scattering for the OPAC real refractive index, and at 12-14 μm, for the quartz band. Absorption from OPAC is considerably larger than our estimates at the 2.5-8 μm and 11-17 μm spectral ranges, with differences in ω reaching up to 0.6 at several bands. An underestimation of the dust absorption is observed in the window region between 9 and 10 μm, with differences in ω up to 0.15. When looking at the asymmetry factor, OPAC calculations appear in agreement with our results in reproducing the magnitude and the spectral decrease of g.

As expected, the differences between the different samples, and also between our samples and OPAC, considerably increase when the own size distribution for each case is taken into account (Fig. 8b). k_{ext}, ω, and g vary in this case within the range ~0.05-0.35 m^2 g^{-1}, ~0.25-1.0, and ~0.05-0.75, respectively. The largest differences, compared to the results of Fig. 9a, are obtained for N93, due to the combination of a relatively high refractive index and a strong fraction of coarse particles for this sample. Significant differences can be also observed for SOP1-17, especially at ~10 μm and for wavelengths <6 μm, mainly due to the presence of a dominant particle mode centred at 5 μm. SOP1-8, although very rich in coarse particles, presents, in a wide spectral range, the lowest k_{ext} and highest ω (i.e., less absorption), and this is caused by the very low values of the refractive index measured for this sample compared to the other dust cases. However, for the SOP1-8 sample the effect of having a dominant mode of coarse particles strongly influences g, for which the largest values are obtained.

The comparison of our results with those obtained in other studies is very difficult due to the large variety of refractive index and size distribution data used in the literature. McConnell et al. (2010), for instance, have estimated intensive optical properties in the spectral range 0.2-10 μm for Western Saharan dust aerosols based on internal and external mineralogy-based

calculations of the refractive index and aircraft in situ measurements of the particle size distributions. Our results (Fig. 8a) for both k_{ext} and g appear in reasonable agreement (less than about 0.05 absolute difference in mean) with the estimates by McConnell et al. (2010), while lower values (up to 0.2 absolute value difference) are obtained in our study for the single scattering albedo in the window region. In another study, Hansell et al. (2011) have analysed the variability of k_{ext} as a function of the physico-chemical properties of dust, therefore by testing a large number of models for refractive index and particle size distribution. Their results span a relatively extended interval, with k_{ext} within the 8-12.5 μm spectral region varying between about 0 and 1.2 m^2 g^{-1}. Our results fall in the range of variability reported in that study. Hansell et al. (2011) have also shown that the differences in k_{ext} due to the variability of the refractive index and size may significantly amplify when the effect of the shape of particles is considered in the optical calculations. This aspect deserves to be accounted for in future investigations.

5.2 Implications for satellite remote sensing

The possible impact of the variability of the dust infrared optical properties on the bands used for satellite retrievals has been investigated. The main information used by the different satellite inversion algorithms to estimate various dust parameters, such as optical depth at 10 μm, altitude, or effective radius, is the priori estimate of its spectral infrared optical depth (Pierangelo et al., 2004; Klüser et al., 2011 and 2012). Therefore, to test the satellite sensitivity to dust properties we have focused on the differences between our estimates of k_{ext} and those based on the OPAC model in the window spectral region. The variability of the spectral mass extinction coefficient is, in fact, proportional to the variability of the aerosols spectral optical depth. The calculated k_{ext} within the 8-12.5 μm range is shown in Fig. 9, where also the main bands for dust retrieval in the thermal infrared from the AIRS and IASI satellites are reported. In most cases, with the exception of the channels at ~8 μm, the OPAC k_{ext} is observed to fall approximately at the mean of the ensemble of values estimated in this study. A disagreement up to 0.1 m^2 g^{-1}, corresponding to 50-100% of the OPAC k_{ext} absolute value, is observed with respect to the minimum and maximum of k_{ext} for our samples at the different AIRS and IASI bands. Considerable differences in term of spectral variation are also obtained between the OPAC and our experimental k_{ext}, especially within the 8.5-10 and 11-12.5 μm regions. The results of this simple comparison suggest that the fact of not taking into account the variability of dust properties, i.e., using the OPAC model in satellite inversion

algorithms, is expected to possibly induce a significant source of uncertainty on the dust retrievals.

Dust absorption also affects the satellite retrieval of key land and atmospheric parameters. In Fig. 9, for instance, we also report the two MODIS thermal infrared broadband channels, the 31 and 32 centred at 11 and 12 μm, used to estimate the Sea Surface Temperature (SST). The retrieval scheme for SST uses the estimated brightness temperature at the two channels (BT_{11} and BT_{12}), as well as their calculated difference (BT_{11}-BT_{12}). The absolute value and spectral variations of k_{ext} affect both quantities. The dust effect on the retrieval of BT_{11} and BT_{12} has been reported by several authors to be one of the causes for the observed bias between satellite derived SST and surface measurements (May et al., 1992; Chan and Gao, 2005; Merchant et al., 2006). The OPAC model is not able to reproduce the variability of the k_{ext}, both in terms of absolute intensity and spectral changes, therefore contributing to the uncertainties in SST estimations. For example, the integrated area of k_{ext} over the 11 and 12 μm MODIS bands is 0.089 and 0.087 for OPAC, compared to 0.123 and 0.110 for the maxima of k_{ext} at the two bands (sample N93, green dashed line), and 0.067 and 0.054 for the corresponding k_{ext} minima (samples SOP1-8, light-blue dashed line, and N32, blue dashed line). These results indicate that, with respect to our data, OPAC may underestimate, approximately by a factor 2 and an order of magnitude, respectively, the absolute intensity and the spectral variability of the dust signature at the 11 and 12 μm bands, therefore contributing to the uncertainties on SST estimations.

All these considerations show the necessity for a new optical model to use in place of OPAC, and able to provide a better description of the spectral and regional variability of dust properties. The use of this new model would help increase the accuracy of satellite inversions over regions affected by the presence of dust.

5.3 Implications for dust radiative forcing

k_{ext} data can be also used to provide a first guess approximation of the dust infrared radiative forcing sensitivity to dust properties. To do that, we have decided to focus on the forcing efficiency (FE, W m^{-2} τ^{-1}) which is the key parameter describing the aerosol radiative effect. FE is defined as the ratio between the radiative forcing, generally calculated over the whole solar or infrared broadband ranges, and the aerosol optical depth, usually taken at visible wavelengths. The calculation of the forcing efficiency with respect to the optical depth

between wavelength λ_1 (FE_{λ_1}) and the visible wavelength (FE_{vis}), can be performed through the relation:

$$FE_{\lambda_1} = FE_{vis} \frac{\tau_{vis}}{\tau_{\lambda_1}} \qquad (9).$$

The $\frac{\tau_{vis}}{\tau_{\lambda_1}}$ term is a nonlinear function of the aerosol size and refractive index, and may strongly vary as a function of the intensity of absorption bands at infrared wavelengths. Here we want to test the changes in the dust infrared FE when this is calculated with respect to the optical depth at 8, 10, and 12 μm. For the dust infrared forcing efficiency we have taken as a reference the mean of the cloud-free FE_{vis} values reported by Brindley and Russell (2009) at the top of the atmosphere (TOA) for North Africa (~15 W m^{-2} $(\tau^{-1})_{0.55\mu m}$). Calculations of $FE_{8\mu m}$, $FE_{10\mu m}$, and $FE_{12\mu m}$ have been performed for samples SOP0-47, N32, and N93, for which measurements of the optical depth at 0.50 μm, i.e. the τ_{vis}, were available from AERONET data at the stations. The optical depth at 8, 10, and 12 μm for SOP0-47, N32, and N93 has been calculated as the product between k_{ext} (Fig. 9, dashed curves) and the column dust load, DL (g m^{-2}) estimated for each case. DL has been retrieved as the ratio of the measured $\tau_{0.50\mu m}$ and the $(k_{ext})_{0.50\mu m}$, which in turn has been calculated with the Mie theory considering the measured dust size distribution and assuming a particle refractive index at 0.50 μm of 1.53 - 0.002i. The $\tau_{8\mu m}$, $\tau_{10\mu m}$, and $\tau_{12\mu m}$ obtained and associated FE are reported in Table 4. The dust optical depth at infrared wavelengths varies between a minimum of 0.10 to a maximum of 0.92, with resultant $\tau_{0.50\mu m}$ to $\tau_{8\mu m}$, $\tau_{10\mu m}$, and $\tau_{12\mu m}$ ratios between 1.4 and 3.6. The calculated $FE_{8\mu m}$, $FE_{10\mu m}$, and $FE_{12\mu m}$ are thus up to more than three times larger than $FE_{0.50\mu m}$, with an estimated maximum of 54.0 W m^{-2} τ^{-1}. The forcing efficiency largely varies with the wavelength, and also shows an important sensitivity to the optical properties of dust. Differences of the FE for the three cases are relatively small at 10 μm (~2-4 W m^{-2} τ^{-1}, corresponding to a 9-18% difference), and increases at 8 and 12 μm (up to ~10-12 W m^{-2} τ^{-1}, corresponding to about a 30% difference). Hence, these results underline the significant role of the optical properties in modulating the infrared radiative impact of dust.

6. Conclusions

In this paper we have presented new experimental estimates of the infrared complex refractive index of African mineral dust. The particle refractive index has been derived from laboratory transmission spectra (2.5-25 μm) by applying a retrieval algorithm which combines Mie and Lorentz dispersion theories. Spectroscopy measurements have been performed on five natural dust samples collected at the sites of Banizoumbou (Niger) and Tamanrasset (Algeria) during the AMMA campaign in 2006 and which originated in different Western Saharan and Sahelian source regions. Co-located in situ measurements of the dust size distribution and laboratory analyses of particle mineralogy have been considered together with spectroscopy data in order to relate the spectral features of the refractive index to the physico-chemical properties of the particles. The main results of our study may be summarized as follows:

1. For all the different samples, the measured dust absorption spectra and estimated complex refractive index are strongly sensitive to the mineralogical composition of the particles. The main features of the different spectra follow the signatures of clay species (kaolinite, illite, smectite), with the largest absorption bands observed within the 8-12 μm and 17-25 μm spectral regions. Within the 8-12 μm window, the imaginary part rapidly increases from $\leq$0.001 to peak values of 0.3-0.85, while the real part ranges between 1.1 and 2.0. Above 17 μm, k peaks at 0.45-1.0, and n varies between 1.2 and 2.7. Absorption by quartz and other minor minerals, such as calcium-rich species, arises only when the clay signature becomes very low. Absorption by iron oxides is observed to be almost negligible, in contrast with its crucial role at solar wavelengths (Sokolik and Toon, 1999).
2. Our results show the dust refractive index to significantly vary in magnitude for the five analysed cases. Differences between maxima and minima within the main absorption bands for the different samples may reach 1.0 for n and 0.6 for k, corresponding to ~40% variability for n and changes of a factor 2-3 for k. The variability of n and k is linked to the variability of particle mineralogy, mainly clay amount and speciation, and, to a lesser extent, size distribution, in particular the coarse fraction.
3. The results of this study have been compared with other direct spectroscopy estimates and indirect calculations of the infrared refractive index available in the literature and corresponding to dust collected both close to their source regions and along the path of their atmospheric transport. The comparison indicates the results of our study and literature data are comparable in magnitude. However, when related to our results, literature data appear to fail to reproduce the signatures of main minerals, in particular

clays and quartz. Furthermore, the real and the imaginary parts of the refractive index from some literature studies are found not to verify the Kramers-Kronig relations, and thus are theoretically incorrect. The comparison between our results, from Western Africa, and literature data, from different locations in Europe, Africa, and the Caribbean, nonetheless, confirms the expected large spatio-temporal variability of the infrared refractive index of dust, thus highlighting the necessity for an extended systematic investigation.

5. Aerosol intensive optical properties relevant to radiative transfer (k_{ext}, ω, g), have been calculated for the five analysed dust samples based on their estimated complex refractive index and measured particle size distribution. Results indicate a strong sample-to-sample variability for dust infrared optical properties, with k_{ext}, ω, and g varying within the range 0.05-0.35 m^2 g^{-1}, 0.25-1.0, and 0.05-0.75, respectively, due to the combined changes of both the refractive index and size distribution for the different samples. This observed variability has been tested to possibly have a significant impact on satellite retrievals and dust radiative forcing estimates in the thermal infrared. For instance, in terms of radiative effect, the changes in k_{ext} may determine up to ~10 W m^{-2} τ^{-1} variability in the dust infrared forcing efficiency. These results point out the importance of better characterizing the infrared optical properties of dust in order to more correctly evaluate their impact on the climate system.

Spectral complex refractive index data obtained in this study are made available as supplementary material to this paper for use in remote sensing and radiative transfer calculations. Due to the scarcity of information on the infrared refractive index of desert dust, this new dataset constitutes an important contribution for mineral dust studies on the regional and global scale.

Appendix A. Selection of dust events and identification of their source region

The five dust cases analysed in this study were selected based on their different origin and associated mineralogical composition. Three of them were collected at the Sahelian site of Banizoumbou and the other two at the Saharan site of Tamanrasset.

Samples were taken during different periods corresponding to the different phases of the West Africa Monsoon (WAM) annual cycle and associated AMMA Special Observing Periods (SOPs). For Banizoumbou, one of the dust samples was taken during winter in correspondence of the dry season (January - February 2006, AMMA SOP0; sample ID:

847 SOP0-47), and the other two during the pre-Monsoon season (June 2006, AMMA SOP1;
848 samples ID: SOP1-8 and SOP1-17). Emission of dust from the Sahel seldom occurs during
849 the dry season and aerosols collected at Banizoumbou in that period correspond to transport
850 from Saharan areas (Rajot et al., 2008). The SOP0–47 case sampled during the dry season
851 occurred on the 9th of February 2006. This case was associated to a medium-range transport
852 event originated from the Central-Western part of Niger, between the Algeria-Niger and the
853 Mali-Niger frontier regions (Klaver, 2012). In contrast with the dry season, the pre-Monsoon
854 phase is characterized by a maximum in Sahelian dust emissions (Marticorena et al. 2010).
855 Identification of erosion conditions leading to aeolian emission have been performed by
856 combining surface wind field and aerosol mass/concentration measurements, with the data on
857 sand grain horizontal flow obtained by means of a saltiphone installed in proximity of the
858 sampling site station (Klaver, 2012). Two different local erosion episodes are considered
859 from the pre-monsoon season at Banizoumbou: SOP1-8, which occurred on the 4th of June
860 2006, and SOP1-17, between the 8th and the 9th of June 2006. The SOP1-8 event was
861 identified as the strongest erosion episode of the entire SOP1 period at Banizoumbou, based
862 on the measured surface wind speed (>10 m s^{-1} during the whole event, consistently above
863 the 6 m s^{-1} threshold for local emission estimated by Rajot et al. (2008)) and horizontal dust
864 grain flux (peak at ~700 counts s^{-1}). SOP1-17 was instead a post-erosion event characterized
865 by the advection of dust which was locally emitted at Banizoumbou ~3 hours before the
866 sampling started.

867 Tamanrasset data considered here have been acquired in the second part of 2006, during the
868 Monsoon season (July - August 2006, AMMA SOP2; sample ID: N32), and the end of the
869 Monsoon, during the Inter Tropical Convergence Zone (ITCZ) retreat (October – November
870 2006; sample ID: N93). As discussed by Cuesta et al. (2008), local dust production at
871 Tamanrasset (over the Hoggar massif) is very low, and most aeolian dust over this area is
872 transported from a variety of different source regions as a result of different dust lifting
873 mechanisms (e.g., low-level jets, cold pools, or topographic flows). The event considered
874 here in correspondence of the Monsoon season over the Sahel occurred between the 21st and
875 the 27th of July 2006. The dust event originated at the Algeria-Niger frontier and was caused
876 by the succession of three cold pools outflows generated by Mesoscale Convective Systems
877 (MCS). The ITD (Inter-Tropical Discontinuity) organized the three cold pools in a dust front,
878 which propagated northwards to Tamanrasset (Cuesta et al., 2009a). The N32 sample was
879 taken only in the first part of the episode, between the 23rd and the 24th of July. The origin of

the N93 post-Monsoon dust event over Tamanrasset, instead, was associated to an intrusion of the Sub Tropical Westerly Jet (STWJ) into Morocco and North-Western Algeria, which led to the formation of downslope winds along the Saharan side of Atlas Mountains. These winds induced the formation of a dust front which moved southward reaching Tamanrasset between the 5th and the 7th of October 2006 (N93 sample taken throughout the whole event, between the 5th and the 7th of October) (see Cuesta et al., 2008 and supplementary material). For both events (during and after the Monsoon season over the Sahel), the transport time from the source regions to the sampling site of Tamanrasset was estimated to be about 1 day.

Appendix B. Estimation of dust mineralogical composition.

Starting from the measurements described in Section 2.2 (WD-XRF, XRD, CBD, XANES, and EXAFS), the mineralogical composition of the different dust samples has been estimated through the following procedure.

At first, the Total Dust Mass (TDM) collected on the filters has been determined. For samples SOP0-47, SOP1-8, and SOP1-17, the TDM has been obtained directly from an on-line Tapering Element Oscillating Microbalance (TEOM, model 1400a, Rupprecht and Patashnick Albany, USA; 5% uncertainty) available at Banizoumbou (Rajot et al., 2008). These measurements were not available at Tamanrasset. Another possible approach to estimate the TDM consists in calculating it based on the XRF measured elemental composition. XRF analysis was not possible on N32 and N93 samples due to the high amount of dust particles deposited on the filters. We therefore considered four filters sampled immediately before and after the N32 and N93 events. For these filters, for which elemental composition was available from XRF analysis, the TDM was estimated as described in Formenti et al. (2014). Co-located Level 2.0 AERONET measurements at 0.50 μm obtained at Tamanrasset (Cuesta et al., 2008) allowed the estimation of an average aerosol optical depth ($\bar{\tau}$) for these cases. A linear relationship (y=*b*x) between TDM and $\bar{\tau}$ can be established for these filters (R^2=0.87) with *b* = (3122 ± 367) μg. The *b* obtained has then been used, together with the measured $\bar{\tau}$ (see Table 1), to extrapolate the TDM for the N32 and N93 events. The uncertainty on the TDM obtained is ~12%. This procedure for the estimation of the TDM assumes the existence of a proportionality relation between the dust mass (sampled at the ground) and the aerosol optical depth (measured over the whole atmospheric column). This hypothesis can be considered valid at Tamanrasset where the distribution of

dust particles has been observed to be generally uniform within the Saharan Atmospheric Boundary Layer, SABL (from a maximum altitude of ~6 km down to the ground) (Cuesta et al., 2008 and 2009b). CALIPSO lidar transects (http://www-calipso.larc.nasa.gov/products/lidar) passing very close to Tamanrasset in correspondence with the two considered dust events also confirm this assumption.

As a second step, the apportionment of the TDM between the different minerals has been evaluated in the following way:

1) the mass of quartz (with an uncertainty (σ) of ±3%), calcium-rich species (calcite, σ =±3%, dolomite, σ=±10%, gypsum, σ=±5%), and feldspars (orthose, σ=±7%, albite, σ=±2%) have been estimated, both for the Banizoumbou and the Tamanrasset samples, from XRD analysis by applying the calibration coefficients reported in Klaver et al. (2011) and Formenti et al. (2014);
2) the mass of iron oxides has been obtained from CBD (σ=±10%) for the SOP0-47, SOP1-8, and SOP1-17. For the N32 and N93 cases, instead, the iron oxide content has been estimated from the elemental Fe assuming the ratio between the iron in the form of oxide and the total elemental Fe to be 0.59 (Formenti et al., 2008). The Fe content of the N32 and N93 events has been calculated with a procedure similar to that used for the TDM, i.e. by performing a linear fit (y=*d*x) of the measured Fe and $\bar{\tau}$ for the four dust samples obtained before and after the two considered events. The result in this case is d = (142 ± 18) μg, with a correlation R^2= 0.87. The uncertainty on the iron oxide content estimated through this procedure is ~12%. For the SOP1-17 sample only, the speciation between hematite and goethite has been also determined through XANES and EXAFS analyses;
3) the mass of clays (kaolinite, illite, smectite, chlorite), which cannot be directly determined from XRD data due to the absence of appropriated calibration standards for these components, has been estimated as the difference between TDM and the total mass of quartz, calcium-rich species, feldspars, and iron oxides. The mass apportionment between the different clays species can be performed when only kaolinite (K) and illite (I) are present. In this case the mass of the two clays can be separated by the knowledge of their ratio I/K, as estimated by Caquineau et al. (2002). For SOP0-47, SOP1-8, and SOP1-17, the I/K ratio was set at 0.1. For the N32 and N93 samples, instead, also smectite was detected in XRD spectra and the mass apportionment between the different clay species cannot be done. The uncertainty on the estimated total clay mass, calculated with the error

propagation formula including the uncertainties on TDM and the other identified mineral species, varies between 8 and 20%.

Acknowledgements

This work was supported by the Centre National des Etudes Spatiales (CNES). Based on a French initiative, AMMA was built by an international scientific group and is currently funded by a large number of agencies, especially from France, the United Kingdom, the United States, and Africa. It has been the beneficiary of a major financial contribution from the European Community's Sixth Framework Research Programme. Detailed information on scientific coordination and funding is available on the AMMA International Web site at www.amma-international.org. The Tamanrasset AMMA supersite deployment and operation were supported by the Office National de la Météorologie (ONM) in Algeria, the Laboratoire de Météorologie Dynamique (LMD), and the Laboratoire Atmosphères, Milieux, Observations Spatiales (LATMOS). Thanks are also due to the LISA personnel who participated in field campaigns and helped with sample collection and analyses. Helpful comments and suggestions by two anonymous reviewers and the editor are also acknowledged.

977 **References**

978 Ackerman, S. A., and Chung, H.: Radiative effects of airborne dust on regional energy budgets at the
979 top of the atmosphere, J. Appl. Meteorol., 31, 223–233, 1992.
980 Ackerman, S. A.: Remote sensing aerosols using satellite infrared observations, J. Geophys. Res.,
981 102, 17,069– 17,080, 1997.
982 Balkanski, Y., Schulz, M., Claquin, T., and Guibert, S.: Reevaluation of Mineral aerosol radiative
983 forcings suggests a better agreement with satellite and AERONET data, Atmos. Chem. Phys., 7,
984 81–95, doi:10.5194/acp-7-81-2007, 2007.
985 Banks, J. R., and Brindley, H. E.: Evaluation of MSG-SEVIRI mineral dust retrieval products over
986 North Africa and the Middle East, Rem. Sens. Environ., 128, 58-73, 2013.
987 Ben-Ami, Y., Koren, I., and Altaratz, O.: Patterns of North African dust transport over the Atlantic:
988 winter vs. summer, based on CALIPSO first year data, Atmos. Chem. Phys., 9, 7867-7875,
989 10.5194/acp-9-7867-2009, 2009.
990 Ben-Ami, Y., Koren, I., Rudich, Y., Artaxo, P., Martin, S. T., and Andreae, M. O.: Transport of North
991 African dust from the Bodele depression to the Amazon Basin: a case study, Atmos. Chem.
992 Phys., 10, 7533–7544, 2010.
993 Bierwirth, E., Wendisch, M., Ehlich, A., Heese, B., Tesche, M., Althausen, D., Schladitz, A., Müller,
994 D., Otto, S., Trautmann, T., Dinter, T., Von Hoyningen-Huene, W., and Kahn, R.: Spectral
995 surface albedo over Morocco and its impact on radiative forcing of Saharan dust, TellusB, 61,
996 252–269, 2009.
997 Bohren, C. E., and Huffman, D. R.: Absorption and Scattering of Light by Small Particles. Wiley,
998 New York, 1983.
999 Brindley, H. E., and Russell, J. E.: An assessment of Saharan dust loading and the corresponding
1000 cloud-free longwave direct radiative effect from geostationary satellite observations, J. Geophys.
1001 Res., 114, D23201, doi:10.1029/2008JD011635, 2009.
1002 Capelle, V., Chédin, A., Siméon, M., Tsamalis, C., Pierangelo, C., Pondrom, M., Armante, R.,
1003 Crevoisier, C., Crepeau, L., and Scott, N. A.: Evaluation of IASI derived dust aerosols
1004 characteristics over the tropical belt, Atmos. Chem. Phys. Discuss., 13, 30143-30186,
1005 doi:10.5194/acpd-13-30143-2013, 2013.
1006 Caquineau, S., Magonthier, M. C., Gaudichet, A., and Gomes, L.: An improved procedure for the X-
1007 ray diffraction analysis of low-mass atmospheric dust samples, Eur. J. Mineral., 9, 157–166:
1008 1997.
1009 Caquineau, S., Gaudichet, A., Gomes, L., and Legrand, M.: Mineralogy of Saharan dust transported
1010 over northwestern tropical Atlantic Ocean in relation to source regions, J. Geophys. Res.,
1011 107(D15), 4251, doi:10.1029/2000JD000247. 2002.
1012 Carlson, T. N,. and Benjamin, ST. G.: Radiative heating rates for Saharan dust, J. Atmos. Sc., 193-
1013 213, 1980.
1014 Carslaw, K. S., Boucher, O., Spracklen, D. V., Mann, G. W., Rae, J. G. L., Woodward, S., and
1015 Kulmala, M.: A review of natural aerosol interactions and feedbacks within the Earth system,
1016 Atmos. Chem. Phys., 10, 1701-1737, doi:10.5194/acp-10-1701-2010, 2010.
1017 Casasanta, G., di Sarra, A. G., Meloni, D., Monteleone, F., Pace, G., Piacentino, S, and Sferlazzo, D:
1018 Large aerosol effects on ozone photolysis in the Mediterranean, Atmos. Env., 45, 3937-3943,
1019 2011.
1020 Chan, P. K., and Gao, B. J.: A comparison of MODIS, NCEP, and TMI sea surface temperature
1021 datasets, IEEE Geosci. Remote Sens. Lett., 2(3), 270-274,doi: 10.1109/LGRS.2005.846838,
1022 2005.
1023 Claquin, T., Schulz, M., Balkanski, Y. J., and Boucher, O.: Uncertainties in assessing radiative
1024 forcing by mineral dust, TellusB, 50, 491–505, 1998.
1025 Claquin, T., Schulz, M., and Balkanski, Y. J.: Modeling the mineralogy of atmospheric dust sources.,
1026 J. Geophys. Res., 104, 22243-22256, 1999.
1027 Cuesta, J., Edouart, D., Mimouni, M., Flamant, P. H., Loth, C., Gibert, F., Marnas, F., Bouklila, A.,
1028 Kharef, M., Ouchène, B., Kadi, M., and Flamant, C.: Multiplatform observations of the seasonal
1029 evolution of the Saharan atmospheric boundary layer in Tamanrasset, Algeria, in the framework

of the African Monsoon Multidisciplinary Analysis field campaign conducted in 2006, J. Geophys. Res., 113, D00C07, doi:10.1029/2007JD009417, 2008.
Cuesta, J. Lavaysse, C., Flamant, C., Mimouni, M., and Knippertz, P.: Northward bursts of the West African monsoon leading to rainfall over the Hoggar Massif, Algeria, Q. J. R. Meteorol. Soc., doi: 10.1002/qj.439, 2009a.
Cuesta, J., Marsham, J. H., Parker, D. J., and Flamant, C.: Dynamical mechanisms controlling the vertical redistribution of dust and the thermodynamic structure of the West Saharan atmospheric boundary layer during summer, Atmos. Sci. Let., 10: 34–42, 2009b.
D'Almeida, G. A., Koepke, P., and Shettle, E. P.: Atmospheric Aerosols: Global Climatology and Radiative Characteristics, A. Deepak Publishing, 561 pp., 1991.
DeSouza-Machado, S. G., Strow, L. L., Hannon, S. E., and Motteler, H. E.: Infrared dust spectral signatures from AIRS, Geophy. Res. Lett., 33(L03801), 1-5, 2006.
Di Biagio, C., di Sarra, A., and Meloni, D.: Large atmospheric shortwave radiative forcing by Mediterranean aerosol derived from simultaneous ground-based and spaceborne observations, and dependence on the aerosol type and single scattering albedo, J. Geophys. Res., 115, D10209, doi:10.1029/2009JD012697, 2010.
di Sarra, A., Di Biagio, C., Meloni, D., Monteleone, F., Pace, G., Pugnaghi, S., and Sferlazzo, D.: Shortwave and longwave radiative effects of the intense Saharan dust event of March 25-26, 2010, at Lampedusa (Mediterranean sea), J. Geophys. Res., 116, D23209, doi:10.1029/2011JD016238, 2011.
Dufresne, J.-L., Gautier, C., Ricchiazzi, P., and Fouquart, Y.: Longwave scattering effects of mineral aerosols, J. Atmos. Sci., 59, 1959–1966, 2002.
Fisher, K.: The optical constants of atmospheric aerosol particles in the 7.5 - 12 μm spectral region, Tellus, XXVIII, 266- 274, 1976.
Formenti, P., Rajot, J. L., Desboeufs, K., Caquineau, S., Chevaillier, S., Nava, S., Gaudichet, A., Journet, E., Triquet, S., Alfaro, S., Chiari, M., Haywood, J., Coe, H., and Highwood, E.: Regional variability of the composition of mineral dust from western Africa: Results from the AMMA SOP0/DABEX and DODO field campaigns, J. Geophys. Res., 113, D00C13, 10.1029/2008jd009903, 2008.
Formenti, P., Schütz, L., Balkanski, Y., Desboeufs, K., Ebert, M., Kandler, K., Petzold, A., Scheuvens, D., Weinbruch, S., and Zhang, D.: Recent progress in understanding physical and chemical properties of African and Asian mineral dust, Atmos. Chem. Phys., 11, 8231-8256, 10.5194/acp-11-8231-2011, 2011a.
Formenti, P., Caquineau, S., Desboeufs, K., Klaver, A., Chevaillier, S., Journet, E., and Rajot, J.L.: Mapping the physico-chemical properties of mineral dust in Western Africa: Mineralogical composition, submitted to Atmos. Chem. Phys. Discuss., 2014.
Fouquart, Y., Bonnel, B., Brogniez, G., Buriez, J. C., Smith, L., Morcrette, J. J.: Observations of Sahara aerosols: Results of ECLATS field experiment. Part II: Broadband radiative characteristics of the aerosols and vertical radiative flux divergence, J. Climate Appl. Meteor. 26, 38-52, 1987.
Fratini, G., Ciccioli, P., Febo, A., Forgione, A. and Valentini, R.: Size-segregated fluxes of mineral dust from a desert area of northern China by eddy covariance, Atmos. Chem. Phys. **7**, 2839–2854, 2007.
Ginoux, P., Prospero, J. M., Gill, T. E., Hsu, N. C., and Zhao, M.: Global-scale attribution of anthropogenic and natural dust sources and their emission rates based on MODIS Deep Blue aerosol products, Rev. Geophys., 50, RG3005, doi:10.1029/2012RG000388, 2012.
Glotch, T. D., Rossman, G.R., and Aharonson, O.: Mid-infrared (5–100 μm) reflectance spectra and optical constants of ten phyllosilicate minerals, Icarus. 192 : 604–622, 2007.
Glotch T. D., and Rossman, G. R.: Mid-infrared reflectance spectra and optical constants of six iron oxide/oxyhydroxide phases, Icarus 204 : 663–671, 2009.
Gomes, L., and Gillette, D. A.: A comparison of characteristics of aerosol from dust storms in central Asia with soil-derived dust from other regions, Atmos. Environ.,27A, 2539-2544.1993.
Hansell, Jr., R. A., Reid, J. S., Tsay, S. C., Roush, T. L., and Kalashnikova, O. V.: A sensitivity study on the effects of particle chemistry, asphericity and size on the mass extinction efficiency of

mineral dust in the earth's atmosphere: from the near to thermal IR, Atmos. Chem. Phys., 11, 1527-1547, doi:10.5194/acp-11-1527-2011, 2011.
Haywood, J., Francis, P., Osborne, S., Glew, M., Loeb, N., Highwood, E., Tanré, D., Myhre, G., Formenti, P., and Hirst, E.: Radiative properties and direct radiative effect of Saharan dust measured by the C-130 aircraft during SHADE: 1. Solar spectrum, J. Geophys. Res., 108(D18), 8577, doi:10.1029/2002JD002687, 2003.
Haywood, J. M., Allan, R. P., Slingo, T., Milton, S., Edwards, J., and Clerbaux, N.: Can desert dust explain the outgoing longwave radiation anomaly over the Sahara during July 2003?, J. Geophys. Res., 110, D05105, doi:10.1029/2004JD005232, 2005.
Heim, M., Mullins, B. J., Umhauer, H., Kasper, G.: Performance evaluation of three optical particle counters with an efficient "multimodal" calibration method, J. Aer. Sci., 39, 1019-1031, 2008.
Heinold, B., Tegen, I., Schepanski, K., and Hellmuth, O.: Dust radiative feedback on Saharan boundary layer dynamics and dust mobilization, Geophys. Res. Lett., 35, L20817, doi:10.1029/2008GL035319, 2008.
Hess, M., Koepke, P., and Schult, I.: Optical properties of aerosols and clouds: The software package OPAC, Bull. Am. Meteorol. Soc, 79, 831–844, 1998.
Highwood, E. J., Haywood, J. M., Silverstone, M. D., Newman, S. M., and Taylor, J. P.: Radiative properties and direct effect of Saharan dust measured by the C-130 aircraft during Saharan Dust Experiment (SHADE): 2. Terrestrial spectrum, J. Geophys. Res., 108(D18), 8578, doi:10.1029/2002JD002552, 2003.
Hsu, N. C., Herman, J. R., and Weaver, C. J.: Determination of radiative forcing of Saharan dust using combined TOMS and ERBE data, J. Geophys. Res., 105(D16), 20,649–20,661, doi:10.1029/2000JD900150, 2000.
Hudson, P. K., Gibson, E. R., Young, M. A., Kleiber, P. D., and Grassian V. H.: Coupled infrared extinction and size distribution measurements for several clay components of mineral dust aerosol, J. Geophys. Res., 113, D01201, doi:10.1029/2007JD008791, 2008a.
Hudson, P. K., Young, M. A., Kleiber, P. D., and Grassian, V. H.: Coupled infrared extinction spectra and size distribution measurements for several non-clay components of mineral dust aerosol (quartz, calcite, and dolomite), Atmos. Environ., 42(24), 5991–5999, doi:10.1016/j.atmosenv.2008.03.046, 2008b.
Huneeus, N., Chevallier, F. and Boucher, O.: Estimating aerosol emissions by assimilating observed aerosol optical depth in a global aerosol model, Atmos. Chem. Phys., 12, 4585–4606, 2012.
Israelevich, P. L., Levin, Z., Joseph, J. H., and Ganor, E.: Desert aerosol transport in the Mediterranean region as inferred from the TOMS aerosol index, J. Geophys. Res., 107, 4572, doi:10.1029/2001jd002011, 2002.
Iwasaka, Y., Shi, G.-Y. Shen, Z., Kim, S., Trochkin, D., et al.: Nature of atmospheric aerosols over the desert area in the Asian continent: chemical state and number concentration of particles measured at Dunhuang, China, Water, Air Soil Pollut.: Focus 3, 129–145, 2003.
Kalashnikova, O. V., and Sokolik, I. N.: Importance of shapes and compositions of wind-blown dust particles for remote sensing at solar wavelengths, Geophys. Res. Lett., 29, 10, 2002.
Kandler, K., Schütz, L., Deutscher, C., Ebert, M., Hofmann, H., Jäckel, S., Jaenicke, R., Knippertz, P., Lieke, K., Massling, A., Petzold, A., Schladitz, A.,Weinzierl, B.,Wiedensohler, A., Zorn, S., and Weinbruch, S.: Size distribution, mass concentration, chemical and mineralogical composition and derived optical parameters of the boundary layer aerosol at Tinfou, Morocco, during SAMUM 2006, Tellus B, 61, 32–50, doi:10.1111/j.1600-0889.2008.00385.x, 2009.
Kishcha, P., Alpert, P., Barkan, J., Kirchner, I., and Machenhauer, B.: Atmospheric response to Saharan dust deduced from ECMWF reanalysis (ERA) temperature increments, TellusB, 55, 901–913, 2003.
Klaver, A., Formenti, P., Caquineau, S., Chevaillier, S., Ausset, P., Calzolai, G., Osborne, S., Johnson, B., Harrison, M., and Dubovik, O.: Physico-chemical and optical properties of Sahelian and Saharan mineral dust: in situ measurements during the GERBILS campaign, Q. J. R. Meteorol. Soc., 137, 1193-1210, 10.1002/qj.889, 2011.
Klaver, A.: Estimation des propriétés optiques des poussières désertiques d'origines saharienne et sahélienne, à proximité de leurs zones sources d'émission, à partir de leurs propriétés physico-chimiques, PhD thesis, Université Paris VII, 2012.

1139 Klüser, L., and Holzer-Popp, T.: Relationships between mineral dust and cloud properties in the West
1140 African Sahel, Atmos. Chem. Phys., 10, 6901–6915, doi:10.5194/acp-10-6901-2010, 2010.
1141 Klüser, L., Martynenko, D., and Holzer-Popp, T.: Thermal infrared remote sensing of mineral dust
1142 over land and ocean: a spectral SVD based retrieval approach for IASI, Atmos. Meas. Tech., 4,
1143 757–773, 2011.
1144 Klüser, L., Kleiber, P., Holzer-Popp, T., and Grassian, V. H.: Desert Dust Observation From Space –
1145 Application of Measured Mineral Component Infrared Extinction Spectra, Atmos. Environ., 54,
1146 419-427, 2012.
1147 Koepke, P., Hess, M., Schult, I., and Shettle, E. P.: Global aerosol dataset, Report N 243, Max-Plank-
1148 Institut für Meteorologie, Hamburg, 44 pp., 1997.
1149 Lafon S., Rajot, J. L., Alfaro, S. C., and Gaudichet, A.: Quantification of iron oxides in desert aerosol,
1150 Atmos. Environ., 38, 1211–1218, 2004.
1151 Laskina, O., Young, M. A., Kleiber, P. D., and Grassian, V. H.: Infrared extinction spectra of mineral
1152 dust aerosol: Single components and complex mixtures, J. Geophys. Res., 117, D18210,
1153 doi:10.1029/2012JD017756, 2012.
1154 Laurent, B., Marticorena, B., Bergametti, G., Léon, J. F., and Mahowald, N. M.: Modeling mineral
1155 dust emissions from the Sahara desert using new surface properties and soil database, J.
1156 Geophys. Res., 113, D14218, 10.1029/2007jd009484, 2008.
1157 Legrand M., Plana-Fatto, A., and N'Doumé, C.: Satellite detection of dust using the IR imagery of
1158 Meteosat1. Infrared difference dust index, J. Geophys. Res., 106 : 18251-18274, 2001.
1159 Levin, Z., and Lindberg, J.D.: Size distribution, chemical composition and optical properties of urban
1160 and desert aerosols in Israel, J. Geophys. Res.,8 4, 6941-6950, 1979.
1161 Liu, Y. and Daum, P.: The effect of refractive index on size distributions and light scattering
1162 coefficients derived from optical particle counters, J. Aerosol Sci., 31, 945–957, 2000.
1163 Long L. L., Querry, M. R., Bell, R. J., and Alexander, R. W.: Optical properties of calcite and gypsum
1164 in crystalline and powdered form in the infrared and far-infrared, Infrared Physics, 34, 191-201,
1165 1993.
1166 Longtin, D. R., Shettle, E. P., Hummel, J. R. and Pryce, J. D.: A Wind Dependent Desert Aerosol
1167 Model: Radiative Properties, AFGL-TR-88-0112, Air Force Geophysics Laboratory, Hanscom
1168 AFB, MA, 1988.
1169 Maring, H., Savoie, D. L., Izaguirre, M. A., McCormick, C., Arimoto, R., Prospero, J. M., and Pilinis,
1170 C.: Aerosol physical and optical properties and their relationship to aerosol composition in the
1171 free troposphere at izana, tenerife, canary islands, during July 1995, J. Geophys. Res.-Atmos.,
1172 105, 14677–14700, 2000.
1173 Maring, H., Savoie, D. L., Izaguirre, M. A., Custals, L., and Reid, J. S.: Mineral dust aerosol size
1174 distribution change during atmospheric transport, J. Geophys. Res., 108, 8592,
1175 doi:10.1029/2002jd002536, 2003.
1176 Marra, A. C., Blanco, A., Fonti, S., Jurewicz, A., and Orofino, V.: Fine hematite particles of Martian
1177 interest: absorption spectra and optical constants, Journal of Physics: Conference Series, 6, 132–
1178 138, 2005.
1179 Marticorena, B., and Bergametti, G.: Modeling the atmospheric dust cycle: 1. Design of a soil-derived
1180 dust emission scheme, J. Geophys. Res., 100, 16415-16430, 10.1029/95jd00690, 1995.
1181 Marticorena, B., Chatenet, B., Rajot, J. L., Traoré, S., Coulibaly, M., Diallo, A., Koné, I., Maman, A.,
1182 Ndiaye, T., and Zakou, A.: Temporal variability of mineral dust concentrations over West Africa:
1183 analyses of a pluriannual monitoring from the AMMA Sahelian Dust Transect, Atmos. Chem.
1184 Phys., 10, 8899-8915, 10.5194/acp-10-8899-2010, 2010.
1185 Marzo, G. A., Blanco, A., De Carlo, F., D'Elia, M., Fonti, S., Marra, A. C., Orofino, V., and Politi,
1186 R.: The Optical constants of gypsum particles as analog of Martian sulfates, Adv. Sp. Res., 33,
1187 2246–2251, 2004.
1188 May, D. A., Stowe, L. L., Hawkins, J. D., and McClain, E. P.: A correction for Saharan dust effects
1189 on satellite sea surface temperature measurements, J. Geophys. Res., 97(C3), 3611–3619,
1190 doi:10.1029/91JC02987, 1992.
1191 McConnell, C. L., Formenti, P. Highwood, E. J., and Harrison, M. A.: Using aircraft measurements to
1192 determine the refractive index of Saharan dust during the DODO Experiments, Atmos. Chem.
1193 Phys., 10, 3081–3098, doi:10.5194/acp-10-3081-2010, 2010.

1194 Merchant, C. J., Embury, O., Le Borgne, P., and Bellec, B.: Saharan dust in nighttime thermal
1195 imagery: Detection and reduction of related biases in retrieved sea surface temperature, Rem.
1196 Sens. Environ., 104 (1), 15-30, doi: 10.1016/j.rse.2006.03.007, 2006.
1197 Mishchenko, M. I., Liu, L., Travis, L. D., and Lacis, A. A.: Scattering and radiative properties of
1198 semi-external versus external mixtures of different aerosol types, J. Quant. Spectrosc. Ra., 88,
1199 139–147, 2004.
1200 Mooney, T., and Knacke, R.F.: Optical constants of chlorite and serpentine between 2.5 and 50 μm,
1201 Icarus, 64, 493-502, 1985.
1202 Nousiainen, T.: Optical modeling of mineral dust particles: A review, J. Quant. Spectrosc. Ra., 110,
1203 1261–1279, 2009.
1204 Orofino, V., Blanco, A., Fonti, S., Proce, R., and Rotundi, A.: The infrared optical constants of
1205 limestone particles and implications for the search of carbonates on Mars. Planet. Space Sci. 46,
1206 1659–1669, 1998.
1207 Osborne, S. R., Johnson, B. T., Haywood, J. M., Baran, A. J., Harrison, M. A. J., and McConnell, C.
1208 L.: Physical and optical properties of mineral dust aerosol during the Dust and Biomass-burning
1209 Experiment, J. Geophys. Res., 113, D00C03, doi:10.1029/2007jd009551, 2008.
1210 Otto, S., de Reus, M., Trautmann, T., Thomas, A., Wendisch, M., and Borrmann, S.: Atmospheric
1211 radiative effects of an in situ measured Saharan dust plume and the role of large particles, Atmos.
1212 Chem. Phys., 7, 4887–4903, 2007.
1213 Patterson, E. M., Optical Properties of the Crustal Aerosol Relation to Chemical and Physical
1214 Characteristics, J. Geophys. Res., 86, 3236-3246, 1981.
1215 Peterson, J. T., and Weinman, J. A.: Optical properties of quartz dust particles at infrared
1216 wavelengths, Geophys. Res. Lett., 74, 6947-6952, 1969.
1217 Petzold, A., Rasp, K., Weinzierl, B., Esselborn, M., Hamburger, T., Dörnbrack, A., Kandler, K.,
1218 Schötz, L., Knippertz, P., Fiebig, M., and Virkkula, A.: Saharan dust absorption and refractive
1219 index from aircraft-based observations during SAMUM 2006, Tellus B, 61, 118–130,
1220 doi:10.1111/j.1600-0889.2008.00383.x, 2009.
1221 Pierangelo, C., Chédin, A., Heilliette, S., Jacquinet-Husson, N., and Armante, R.: Dust altitude and
1222 infrared optical depth from AIRS, Atmos. Chem. Phys., 4, 1813–1822, 2004.
1223 Prospero, J. M., Ginoux, P., Torres, O., Nicholson, S. E., and Gill, T. E.: Environmental
1224 characterization of global sources of atmospheric soil dust identified with the Nimbus 7 Total
1225 Ozone Mapping Spectrometer (TOMS) absorbing aerosol product, Rev. Geophys., 40, 2-1–2-31,
1226 2002.
1227 Pujol, J.: The solution of nonlinear inverse problems and the Levenberg-Marquardt method,
1228 Geophysics (SEG) 72 (4): W1–W16. doi:10.1190/1.2732552, 2007.
1229 Pye, K.: Aeolian Dust and Dust Deposits, Academic Press, London, 334 pp., 1987.
1230 Querry, M. R., Osborne, G., Lies, K., Jordon, R., Coveney, R. M.: Complex refractive index of
1231 limestone, Appl. Opt., 17, 353–356, 1978, 1978.
1232 Querry, M.: Optical Constants of Minerals and Other Materials from the Millimeter to the Ultraviolet,
1233 Report CRDEC-CR-88009, US Army, Aberdeen, 1987.
1234 Rajot, J. L., Formenti, P., Alfaro, S., Desboeufs, K., Chevaillier, S., Chatenet, B., Gaudichet, A.,
1235 Journet, E., Marticorena, B., Triquet, S., Maman, A., Mouget, N., and Zakou, A.: AMMA dust
1236 experiment: An overview of measurements performed during the dry season special observation
1237 period (SOP0) at the Banizoumbou (Niger) supersite, J. Geophys. Res., 113, D00C14,
1238 doi:10.1029/2008jd009906, 2008.
1239 Redelsperger, J.-L., Thorncroft, C. D., Diedhiou, A., Lebel, T., Parker, D. J., and Polcher, J.: African
1240 Monsoon Multidisciplinary Analysis: An International Research Project and Field Campaign, B.
1241 Am. Meteorol. Soc., 87, 1739–1746, doi:10.1175/BAMS-87-12-1739, 2006.
1242 Reid, E. A., Reid, J. S., Meier, M. M., Dunlap, M. R., Cliff, S. S., Broumas, A., Perry, K., and
1243 Maring, H.: Characterization of African dust transported to Puerto Rico by individual particle
1244 and size segregated bulk analysis, J. Geophys. Res., 108, 8591, 10.1029/2002jd002935, 2003.
1245 Rosenfeld, D., Rudich, Y, and Lahav, R.: Desert dust suppressing precipitation: A possible
1246 desertification feedback loop, Proc. Natl. Acad. Sci. U. S. A., 98, 5975–5980,
1247 doi:10.1073/pnas.101122798, 2001.

Roush, T., Pollack, J., and Orenberg, J.: Derivation of midinfrared (5–25 μm) optical constants of some silicates and palagonite. Icarus 94, 191–208, 1991.
Saikia, B., and Parthasarathy, G.: Fourier Transform Infrared Spectroscopic Characterization of Kaolinite from Assam and Meghalaya, Northeastern India, J. Mod. Phys., 2010, 1, 206-210, 2010.
Schütz, L., Jaenicke, R., and Pietrek, H.: Saharan dust transport over the North Atlantic Ocean, Spec. Pap. Geol. Soc. Am., 186, 87–100, 1981.
Shettle, E. P. and Fenn, R. W.: Models of the atmospheric aerosols and their optical properties, in AGARD Conference Proceedings n. 183, Optical Propagation in the Atmosphere. Presented at the Electromagnetic Wave Fropagation Panel Symposium. Lyngby, Denmark, 27-31 October 1975. AGARD-CP-183, available from U.S. National Technical Information Service, AD A028-615, 1976.
Shettle, E. P. and Fenn, R. W.: Models for the Aerosols of the Lower Atmosphere and the Effects of Humidity Variations on Their Optical Properties, AFGL-TR-79-0214, ADA085951, 1979.
Slingo, A., Ackerman, T. P., Allan, R. P., Kassianov, E. I., McFarlane, S. A., Robinson, G. J., Barnard, J. C., Miller, M. A., Harries, J. E., Russell, J. E., and Dewitte, S.: Observations of the impact of a major Saharan dust storm on the atmospheric radiation balance, Geophys. Res. Lett., 33, L24817, doi:10.1029/2006GL027869, 2006.
Sokolik, I. N., Andronova, A., and Johnson, T. C.: Complex refractive index of atmospheric dust aerosols, Atmos. Env., 27A, 2495-2502, 1993.
Sokolik, I. N., and Toon, O. B.: Direct radiative forcing by anthropogenic airborne mineral aerosols, Nature, 381, 681-683, doi: 10.1038/381681a0, 1996.
Sokolik, I. N., Toon, O. B., Bergstrom, R. W.: Modeling the radiative characteristics of airborne mineral aerosols at infrared wavelengths. Journal of Geophysical Research Letters. 103 : 8813-8826, 1998.
Sokolik, I., and Toon, O.: Incorporation of mineralogical composition into models of the radiative properties of mineral aerosol from UV to IR wavelengths, J. Geophys. Res., 104, 9423-9444, 1999.
Sokolik, I. N.: The spectral radiative signature of wind-blown mineral dust: Implications for remote sensing in the thermal IR region, Geophys. Res. Lett., 29(24), 2154, doi:10.1029/2002GL015910, 2002.
Spitzer, W.G., and Kleinman, D.A.: Infrared lattice bands of quartz. Phys. Rev. 121, 1324–1335, 1961.
Textor, C., et al.: The effect of harmonized emissions on aerosol properties in global models: an AeroCom experiment, Atmos. Chem. Phys., 7, 4489–4501, doi:10.5194/acp-7-4489-2007, 2007.
Toon, O. B., and Pollack, J. B.: A global average model of atmospheric aerosols for radiative transfer calculations, J. Appl. Meteor., 15: 225-246, 1976.
Volz F.E.: Infrared refractive index of atmospheric aerosol substances, Appl. Optics, 11, 755-759, 1972.
Volz, F. E.: Infrared optical constants of ammonium sulfate, Sahara dust; volcanic pumice and flyash, Appl. Optics., 12, 564-568, 1973.
Wang, H., Shi, G., Li., S., Li., W., Wang, B., and Huang, Y.: The impact of optical properties on radiative forcing due to dust aerosols, Adv. Atm. Sci., 23, 431-441, 2006.
World Meteorology Organization (WMO) publication. World Climate Research Program: A preliminary cloudless standard atmosphere for radiation computation, WCP-112, WMO/TD-NO. 24, 1986.
Winfield, K. A.: Factors controlling water retention of alluvial deposits. Western Mojave Desert, available at http://wwwrcamnl.wr.usgs.gov/uzf/winfield.thesis.pdf. Tellus, 2000.

Table captions

Table 1. Main characteristics of the five dust cases selected in this study: the sample ID, the measurement site, the date and time of beginning and end of the observed dust event, the associated filter sampling time interval within the event, and the identified dust source region. The mean aerosol optical depth (τ) at 0.50 μm and the Ångstrom exponent (α, calculated between 0.44 and 0.87 μm) obtained from AERONET measurements during filter sampling for the different cases are also reported; no data are available for the SOP1-8, when the solar zenith angle at the sampling start was >70°, and for the SOP1-17, which corresponds to nighttime data.

Table 2. Mineralogical composition (% by mass) of the five samples from the Banizoumbou and the Tamanrasset sites. The estimated uncertainties associated to the identification of the different mineral species are: clays (±8-20%), quartz (±3%), calcite (±3%), dolomite (±10%), gypsum (±5%), orthose (±7%), albite (±2%), iron oxides (±10-12%).

Table 3. Position of main detected dust infrared band peaks with associated mineral specie and transition assignment.

Table 4. Estimated dust optical depth and TOA forcing efficiency (FE, W m^{-2} τ^{-1}) at 8, 10, and 12 μm for the SOP0-47, N32, and N93 cases (see text for details). The measured τ at 0.50 μm from AERONET is also reported.

Figure captions

Figure 1. Particle number (dN/dlogD) and volume (dV/dlogD) size distributions (normalized with respect to the total number and total volume of particles, respectively) obtained for the five selected dust events. The dots indicate the GRIMM measured values, while the lines are the multimodal lognormal fit data. Black and grey dashed lines are the averages of the volume size distributions for the five samples obtained including (mean_A, black dashed line) and excluding (mean_B, grey dashed line) the largest mode at ~25 μm for N32 and N93 samples. The legend in the bottom panel identifies the line styles used in the plot.

Figure 2. Absorbance spectra measured within the spectral range 2.5-25 μm for the five different dust samples. The legend identifies the line styles used in the plot.

Figure 3. Real (n) and imaginary (k) parts of the complex refractive index within the spectral range 2.5-25 μm for individual minerals composing the dust. References for the plotted curves are: kaolinite (Glotch et al., 2007); illite (Querry, 1987); montmorillonite (a mineral of the smectite family, taken here as representative for this clay species) (Glotch et al., 2007); quartz (Peterson and Weimnman, 1969); calcite (Querry et al., 1978; Long et al., 1993); dolomite (Querry, 1987); gypsum (Long et al., 1993); hematite (Marra et al., 2005); goethite (Glotch and Rossman, 2009). No literature data are available for feldspars (orthose and albite) at infrared wavelengths. The colour code used for the different minerals is indicated in the legend in the bottom panel.

Figure 4. Comparison between the experimental $Q_{abs}(\lambda)/a$ (cm^{-1}) spectra (black curves) and the theoretical ones obtained from the nonlinear fitting procedure (yellow curves). The line styles used in the plot and the number of oscillators for each fit are also indicated in the legends.

Figure 5. Residuals ($R = \frac{(\exp - \mathrm{fit})}{\sigma_{\exp}}$) of the fit normalized by the measurement errors calculated for SOP1-8 and N93. In the residual calculation, exp is the experimental $Q_{abs}(\lambda)/a$, while fit is the $Q_{abs}(\lambda)/a$ obtained from the fitting procedure. The measurement error, σ_{exp}, is 6.4% for SOP1-8 and 5.9% for N93. Red lines indicate the ±1 interval.

Figure 6. Real (n, top panel) and imaginary (k, bottom panel) part of the complex refractive index obtained within the range 2.5 – 25 μm for the five different dust samples. The legend in the top panel identifies the line styles used in the plot.

Figure 7. Comparison of our results with other direct and indirect estimates of the dust refractive index as reported in the literature. The plot reports the real and the imaginary parts of the refractive index for: *1. Volz (1972)* (indicated as VO72 in the plot): rainout dust aerosols collected in Germany and composed of a mixture of soil particles, fly ashes, and pollen (spectroscopy method; also used as the "dust-like" model in Shettle and Fenn, 1979); *2. Volz (1973)* (indicated as VO73): Saharan dust collected at Barbados, West Indies (spectroscopy method); *3. Fouquart et al. (1987)* (indicated as FO87): Saharan sand collected at Niamey, Niger (spectroscopy method); *4. Carlson and Benjamin, (1980), Sokolik et al. (1993)* (indicated as CA80): mineral dust model, as used in the OPAC and GADS databases (based on a synthesis of measurements on Saharan dust or generally on desert aerosols); 5. *Longtin et al. (1988)* (indicated as LO88): dust sand, i.e. modelled as an internal mixture of hematite (10% by volume) and quartz. In the internal mixing hypothesis the dust refractive index is calculated as the volume average of the refractive indices of individual minerals; *6. OPAC desert model*: modelled as an internal mixture of a water soluble component at 80% relative humidity (5% by volume), and mineral dust in nucleation (3% by volume), accumulation (72% by volume), and coarse (20% by volume) modes (Hess et al., 1998); the dust refractive index for the three modes is that reported by CA80. The region in blue in the plot indicates the range of variability of the results of this study. The legend in the bottom panel identifies the line styles used in the plot for literature data. Refractive index y-axes are located on the left side of the plots, with the only exception of LO88 for which the y-axis is on the right side.

Figure 8. Mass extinction efficiency (k_{ext}, $m^2\ g^{-1}$), single scattering albedo (ω), and asymmetry factor (g) computed with the Mie theory between 2.5 and 25 μm for the five

analysed dust cases. Calculations have been performed by considering for each sample the estimated refractive and (left panel, a) the same size distribution for the five cases, i.e., the mean_B reported in Fig.1, or (right panel, b) the own size distribution measured in correspondence of each sample. By comparison, the spectral optical properties obtained using the OPAC refractive index, calculated considering the mean_B size distribution, are shown in the plot. The legend in the top left panel identifies the line styles used in the plot.

Figure 9. Mass extinction efficiency (k_{ext}, m^2 g^{-1}) calculated for the five dust cases within the 7.5-12.5 μm spectral range. According to Fig. 8, continuous and dashed lines correspond to k_{ext} calculations performed by considering respectively the same size distribution for all dust cases (continuous lines) and the own size distribution corresponding to each sample (dashed lines). Vertical lines and the two shaded areas refer to the following different satellite remote sensing channels: (grey dashed lines) six AIRS channels for dust retrieval in the thermal infrared (8.10, 8.15, 9.31, 10.36, 11.48, 11.86 μm); (black dashed line) IASI channel for dust optical depth retrieval at 10 μm; (grey shaded areas) the two MODIS broadband channels (10.78-11.28 and 11.77-12.27 μm) used for Sea Surface Temperature (SST) estimation.

Tables

Table 1. Main characteristics of the five dust cases selected in this study: the sample ID, the measurement site, the date and time of beginning and end of the observed dust event, the associated filter sampling time interval within the event, and the identified dust source region. The mean aerosol optical depth (τ) at 0.50 µm and the Ångstrom exponent (α, calculated between 0.44 and 0.87 µm) obtained from AERONET measurements during filter sampling for the different cases are also reported; no data are available for the SOP1-8, when the solar zenith angle at the start of the sampling was >70°, and for the SOP1-17, which corresponds to nighttime data.

Sample ID	**Measurement site**	**Dust event period: beginning – end (date and time in UTC)**	**Dust sampling period within the event: beginning – end (date and time in UTC)**	**Dust source**	**$\tau_{0.50\mu m}$ (from AERONET)**	**$\alpha_{0.44\text{-}0.87\mu m}$ (from AERONET)**
SOP0-47	Banizoumbou	09/02/2006 01:50 – 10/02/2006 02:20	09/02/2006 09:28 – 09/02/2006 16:32	Algeria – Niger and Mali – Niger frontier areas	0.52	0.15
SOP1-8	Banizoumbou	04/06/2006 16:52 – 04/06/2006 17:36	04/06/2006 16:52 – 04/06/2006 17:36	Local erosion event	-	-
SOP1-17	Banizoumbou	08/06/2006 22:33 – 09/06/2006 06:40	08/06/2006 22:33 – 09/06/2006 06:40	Local erosion event	-	-
N32	Tamanrasset	21/07/2006 ~21:00 – 27/07/2006 ~18:00	23/07/2006 09:55 – 24/07/2006 11:41	Eastern part of the Algeria – Niger frontier area	1.30	0.06
N93	Tamanrasset	05/10/2006 ~00:00 – 07/10/2006 ~12:00	05/10/2006 13:09 – 07/10/2006 10:40	Algerian Atlas	0.48	0.11

Table 2. Mineralogical composition (% by mass) of the five samples from the Banizoumbou and the Tamanrasset sites. The estimated uncertainties associated to the identification of the different mineral species are: clays (±8-20%), quartz (±3%), calcite (±3%), dolomite (±10%), gypsum (±5%), orthose (±7%), albite (±2%), iron oxides (±10-12%).

Sample ID	Clays			Quartz	Calcium-rich			Feldspars		Iron Oxides	
	Kaolinite	Illite	Smectite		Calcite	Dolomite	Gypsum	Orthose	Albite	Hematite	Goethite
SOP0-47	81%	8%	ND	6%	ND	<1%	<1%	<1%	<1%	4%	
SOP1-8	47%	5%	ND	40%	ND	ND	ND	3%	<1%	4%	
SOP1-17	80%	8%	ND	6%	ND	ND	ND	<1%	ND	1%	4%
N32	90%			5%	<1%	ND	<1%	<1%	<1%	4%	
N93	67%			17%	6%	ND	5%	<1%	<1%	4%	

ND = Not Detected

1422 **Table 3.** Position of main detected dust infrared band peaks with associated mineral species
1423 and transition assignment.

1424

Wavelength (µm)	Wavenumber (cm^{-1})	Mineral specie	Assignment
2.7	3700	kaolinite	OH stretching
2.76	3620	kaolinite	OH stretching
7.0	1431	calcite	$(CO_3)^{2-}$ stretching
8.8	1135	gypsum	SO_4 stretching
9.0	1117	kaolinite, smectite	Si-O stretching
9.2	1092	quartz	Si-O stretching
9.7	1035	illite, kaolinite, smectite	Si-O stretching
9.9	1008	kaolinite	Si-O stretching
10.9	914	kaolinite	Al-OH deformation
11.4	876	calcite	C-O stretching
12.5	800	quartz	Si-O bending
12.9	777	quartz	Si-O bending
18.8	533	kaolinite	Fe-O,Fe_2O_3,Si-O-Al stretching
19.3	519	illite, smectite	Al–O–Si deformation
21.4	468	illite, kaolinite, smectite	Si-O-Si bending
23.1	433	illite, kaolinite	Si-O deformation

1425

1426

1427

1428

1429

1430

1431

1432

1433

1434

1435

1436

1437

Table 4. Estimated dust optical depth and TOA forcing efficiency (FE, W m^{-2} τ^{-1}) at 8, 10, and 12 μm for the SOP0-47, N32, and N93 cases (see text for details). The measured τ at 0.50 μm from AERONET is also reported.

		8 μm		10 μm		12 μm	
	$\tau_{0.50\mu m}$ (from AERONET)	$\tau_{8\mu m}$	$FE_{8\mu m}$	$\tau_{10\mu m}$	$FE_{10\mu m}$	$\tau_{12\mu m}$	$FE_{12\mu m}$
SOP0-47	0.52	0.18	42.6	0.31	25.1	0.20	39.8
N32	1.30	0.36	54.0	0.92	21.2	0.48	40.8
N93	0.48	0.17	43.2	0.31	23.1	0.23	31.1

Figures

Figure 1. Particle number (dN/dlogD) and volume (dV/dlogD) size distributions (normalized with respect to the total number and total volume of particles, respectively) obtained for the five selected dust events. The dots indicate the GRIMM measured values, while the lines are the multimodal lognormal fit data. Black and grey dashed lines are the averages of the volume size distributions for the five samples obtained including (mean_A, black dashed line) and excluding (mean_B, grey dashed line) the largest mode at ~25 µm for N32 and N93 samples. The legend in the bottom panel identifies the line styles used in the plot.

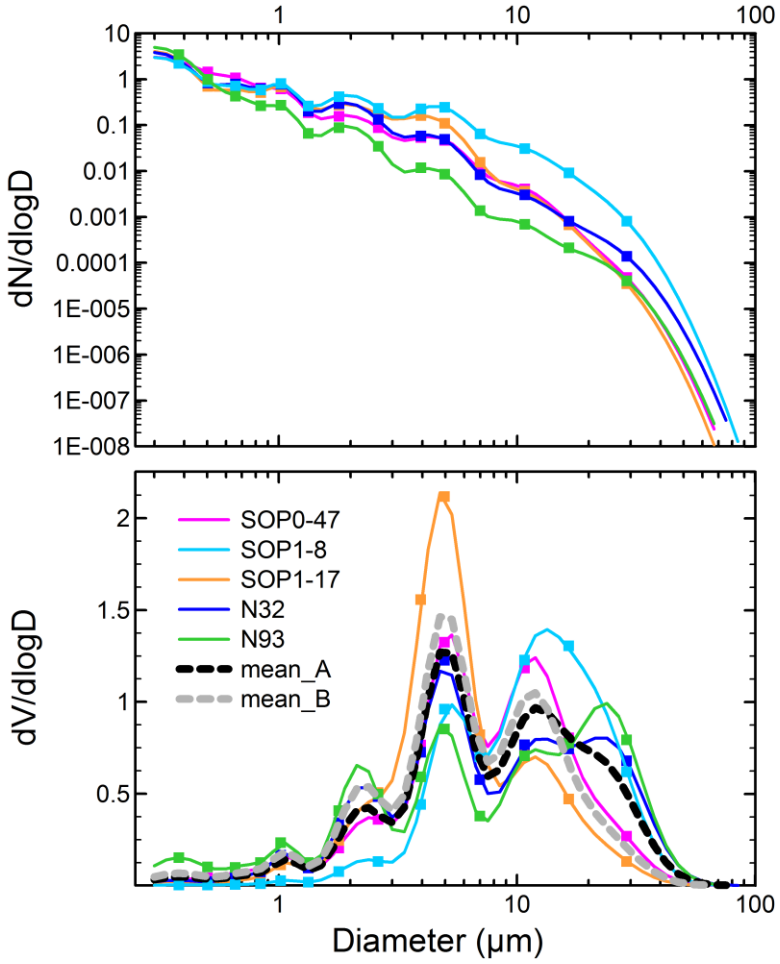

Figure 2. Absorbance spectra measured within the spectral range 2.5-25 µm for the five different dust samples. The legend identifies the line styles used in the plot.

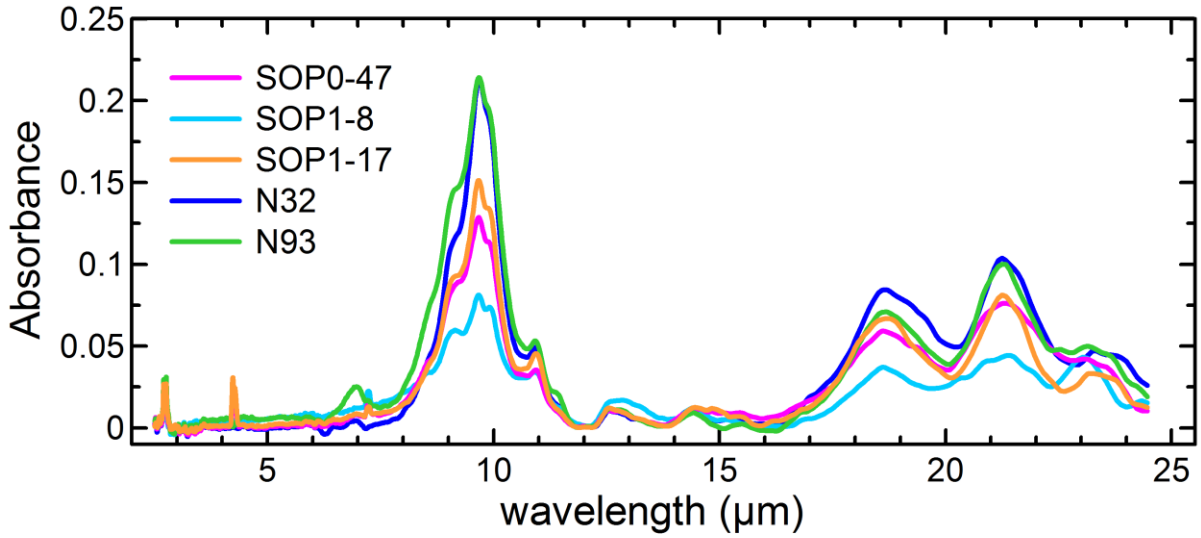

Figure 3. Real (n) and imaginary (k) parts of the complex refractive index within the spectral range 2.5-25 µm for individual minerals composing the dust. References for the plotted curves are: kaolinite (Glotch et al., 2007); illite (Querry, 1987); montmorillonite (a mineral of the smectite family, taken here as representative for this clay species) (Glotch et al., 2007); quartz (Peterson and Weimnman, 1969); calcite (Querry et al., 1978; Long et al., 1993); dolomite (Querry, 1987); gypsum (Long et al., 1993); hematite (Marra et al., 2005); goethite (Glotch and Rossman, 2009). No literature data are available for feldspars (orthose and albite) at infrared wavelengths. The colour code used for the different minerals is indicated in the legend in the bottom panel.

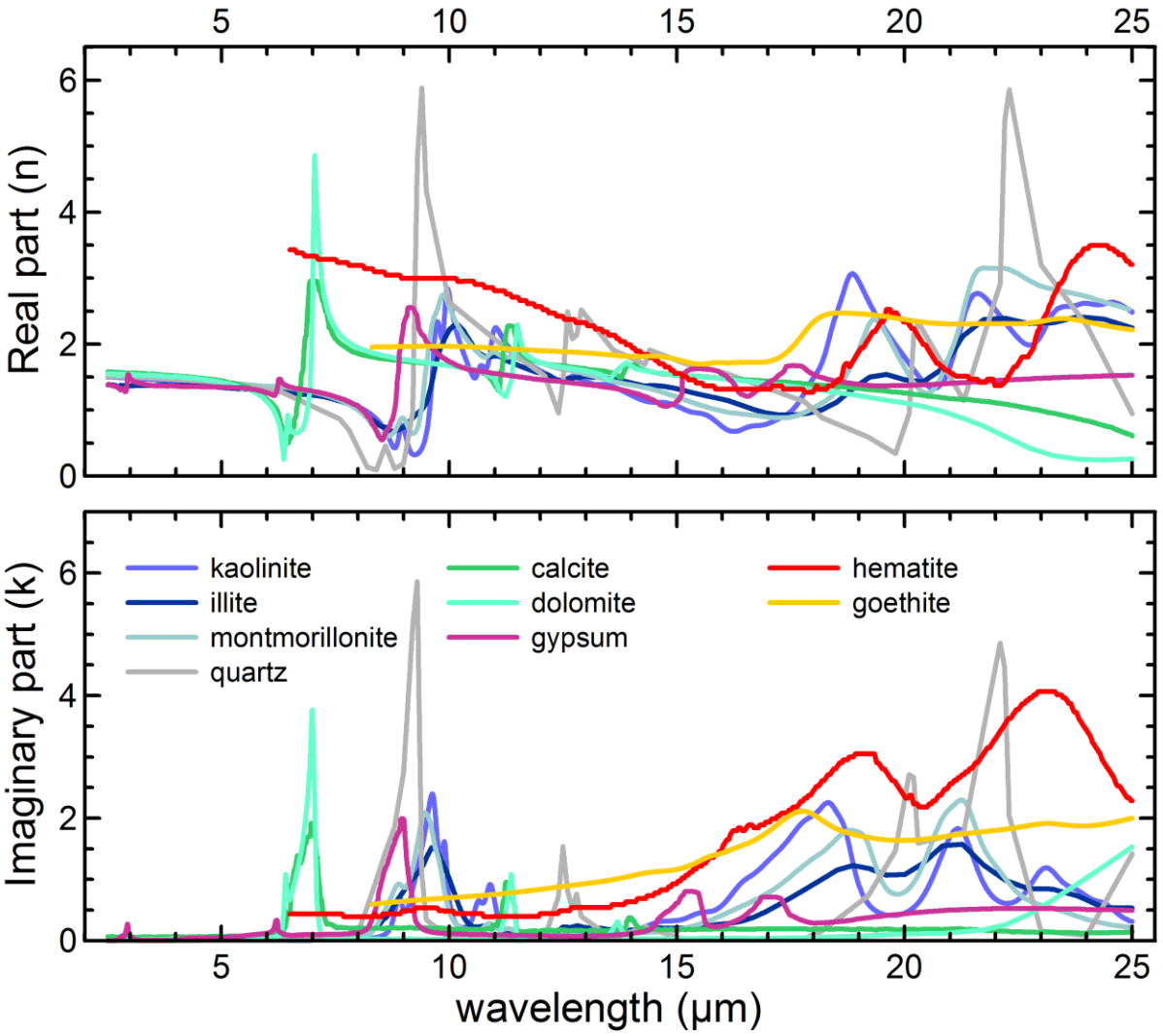

Figure 4. Comparison between the experimental $Q_{abs}(\lambda)/a$ (cm^{-1}) spectra (black curves) and the theoretical ones obtained from the nonlinear fitting procedure (yellow curves). The line styles used in the plot and the number of oscillators for each fit are also indicated in the legends.

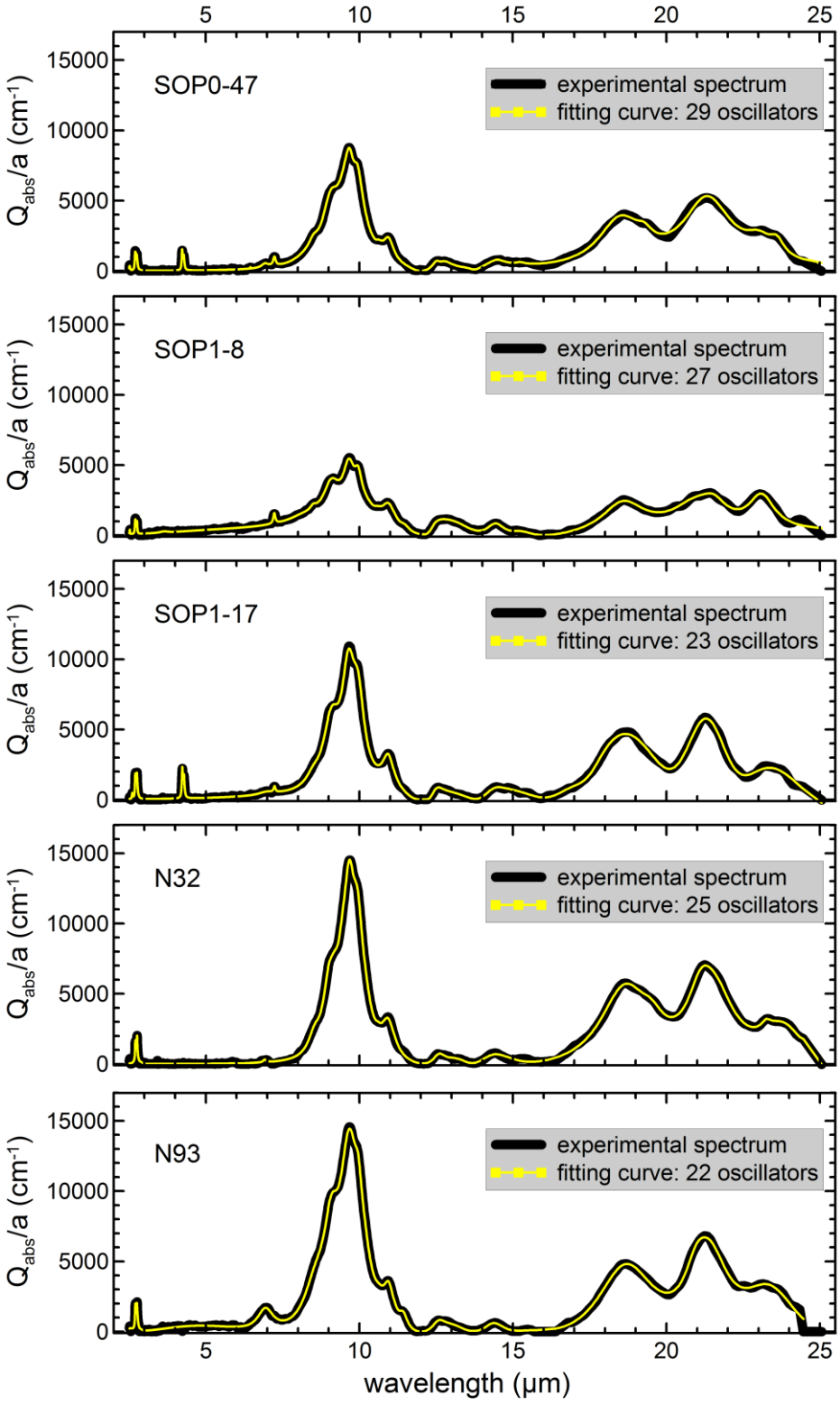

Figure 5. Residuals ($R = \frac{(\exp - \mathrm{fit})}{\sigma_{\exp}}$) of the fit normalized by the measurement errors calculated for SOP1-8 and N93. In the residual calculation, exp is the experimental $Q_{abs}(\lambda)/a$, while fit is the $Q_{abs}(\lambda)/a$ obtained from the fitting procedure. The measurement error, σ_{exp}, is 6.4% for SOP1-8 and 5.9% for N93. Red lines indicate the ±1 interval.

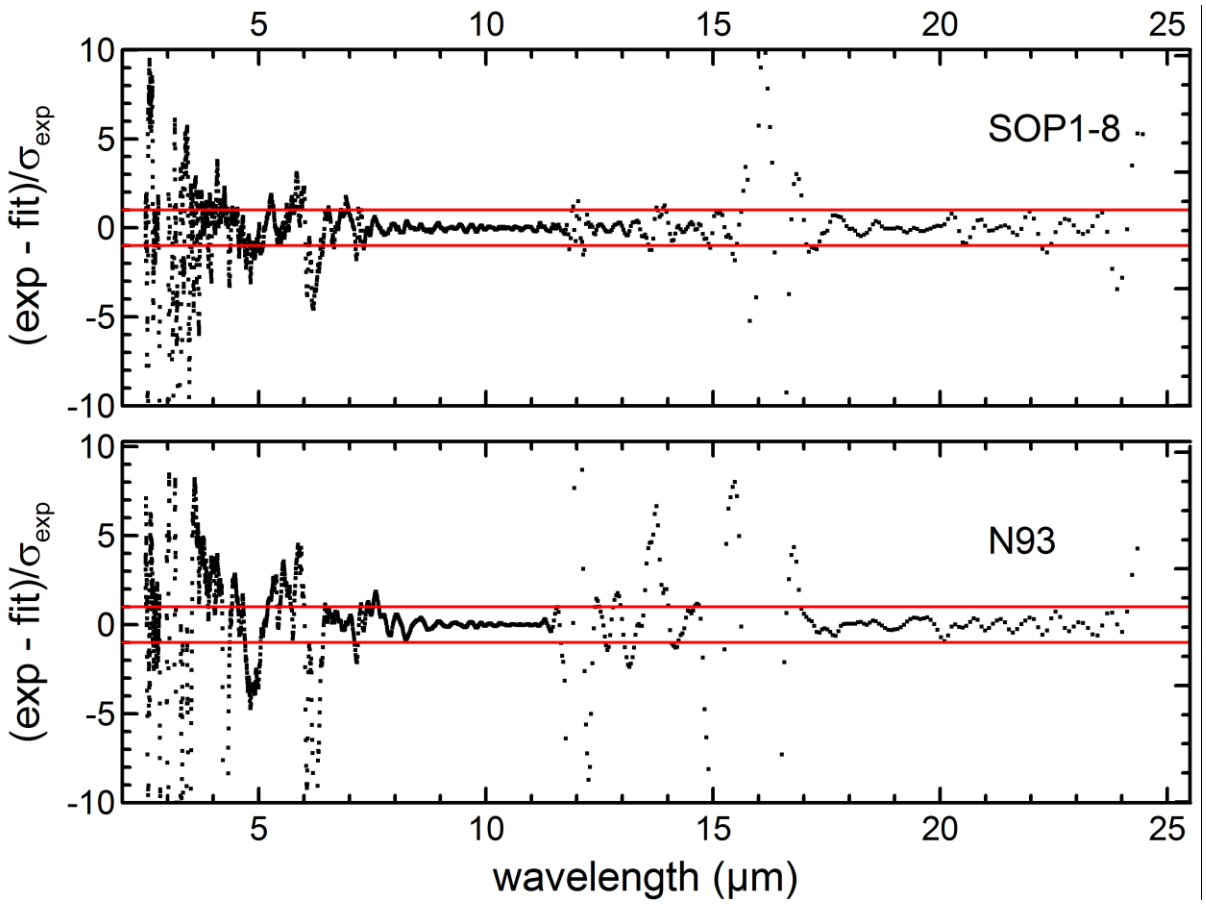

Figure 6. Real (n, top panel) and imaginary (k, bottom panel) part of the complex refractive index obtained within the range 2.5 – 25 µm for the five different dust samples. The legend in the top panel identifies the line styles used in the plot.

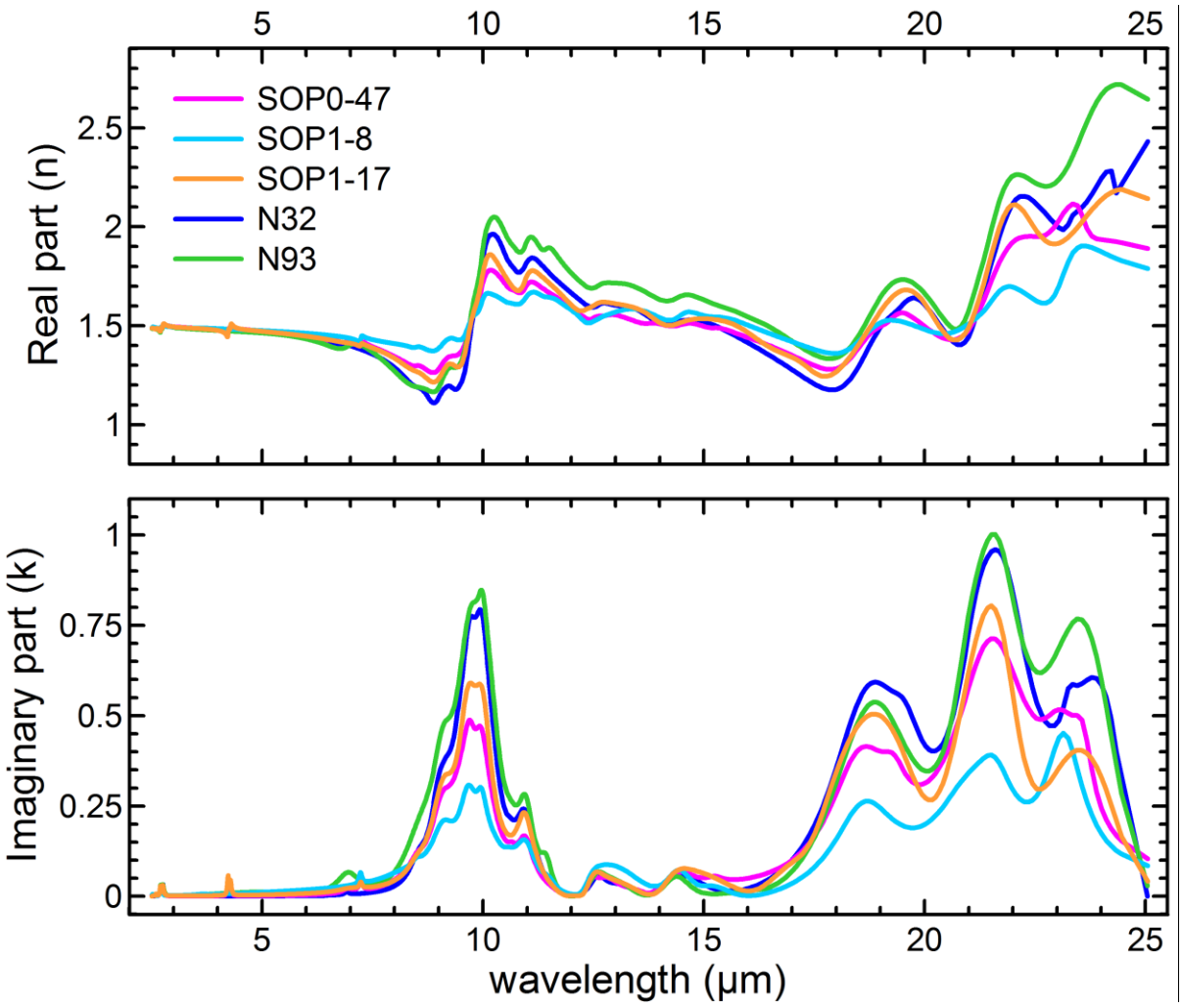

Figure 7. Comparison of our results with other direct and indirect estimates of the dust refractive index as reported in the literature. The plot reports the real and the imaginary parts of the refractive index for: *1. Volz (1972)* (indicated as VO72 in the plot): rainout dust aerosols collected in Germany and composed of a mixture of soil particles, fly ashes, and pollen (spectroscopy method; also used as the "dust-like" model in Shettle and Fenn, 1979); *2. Volz (1973)* (indicated as VO73): Saharan dust collected at Barbados, West Indies (spectroscopy method); *3. Fouquart et al. (1987)* (indicated as FO87): Saharan sand collected at Niamey, Niger (spectroscopy method); *4. Carlson and Benjamin, (1980), Sokolik et al. (1993)* (indicated as CA80): mineral dust model, as used in the OPAC and GADS databases (based on a synthesis of measurements on Saharan dust or generally on desert aerosols); 5. *Longtin et al. (1988)* (indicated as LO88): dust sand, i.e., modelled as an internal mixture of hematite (10% by volume) and quartz. In the internal mixing hypothesis the dust refractive index is calculated as the volume average of the refractive indices of individual minerals; *6. OPAC desert model*: modelled as an internal mixture of a water soluble component at 80% relative humidity (5% by volume), and mineral dust in nucleation (3% by volume), accumulation (72% by volume), and coarse (20% by volume) modes (Hess et al., 1998); the dust refractive index for the three modes is that reported by CA80. The region in blue in the plot indicates the range of variability of the results of this study. The legend in the bottom panel identifies the line styles used in the plot for literature data. Refractive index y-axes are located on the left side of the plots, with the only exception of LO88 for which the y-axis is on the right side.

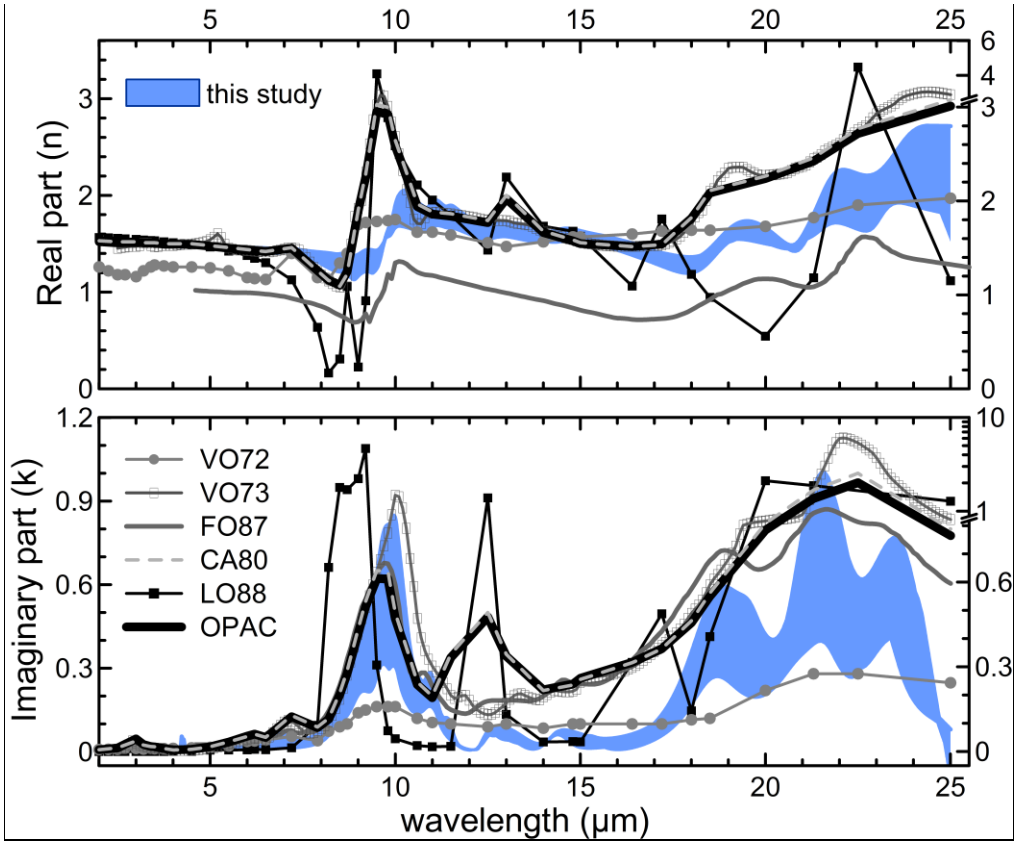

Figure 8. Mass extinction efficiency (k_{ext}, m^2 g^{-1}), single scattering albedo (ω), and asymmetry factor (g) computed with the Mie theory between 2.5 and 25 µm for the five analysed dust cases. Calculations have been performed by considering for each sample the estimated refractive and (left panel, a) the same size distribution for the five cases, i.e., the mean_B reported in Fig.1, or (right panel, b) the own size distribution measured in correspondence of each sample. By comparison, the spectral optical properties obtained using the OPAC refractive index, calculated considering the mean_B size distribution, are shown in the plot. The legend in the top left panel identifies the line styles used in the plot.

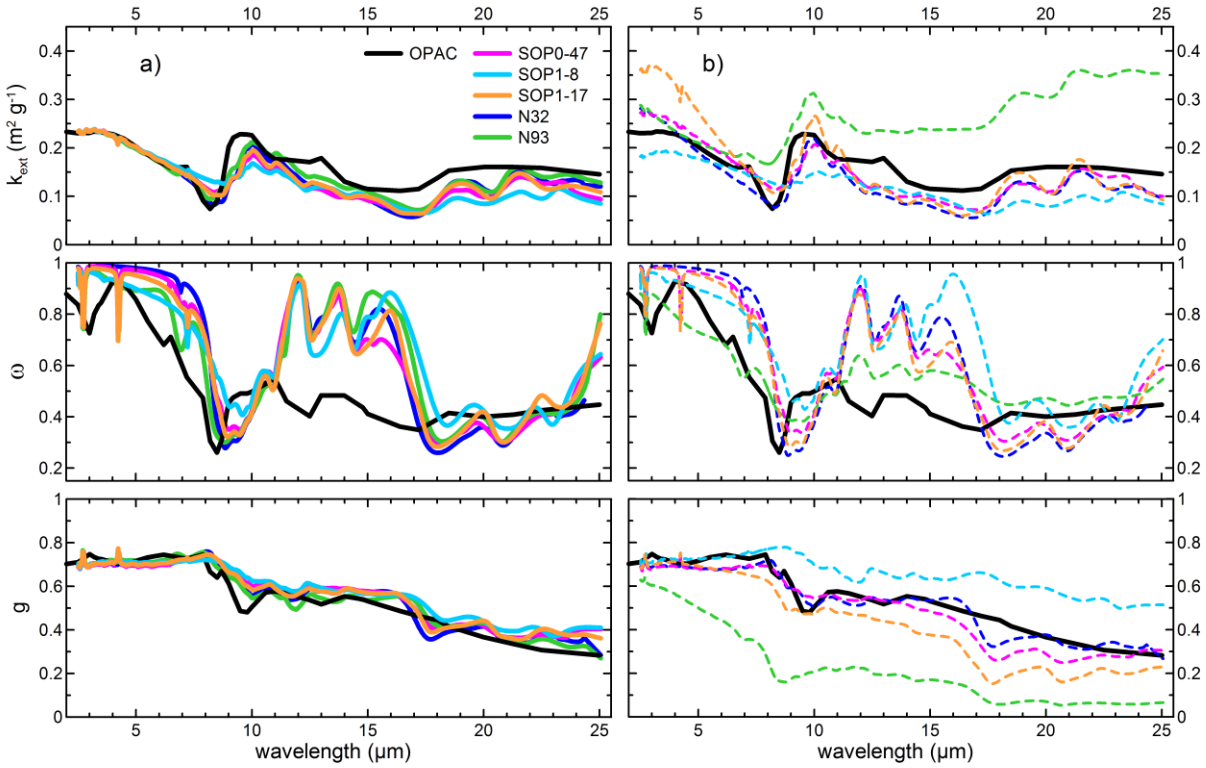

Figure 9. Mass extinction efficiency (k_{ext}, m^2 g^{-1}) calculated for the five dust cases within the 7.5-12.5 µm spectral range. According to Fig. 8, continuous and dashed lines correspond to k_{ext} calculations performed by considering respectively the same size distribution for all dust cases (continuous lines) and the own size distribution corresponding to each sample (dashed lines). Vertical lines and the two shaded areas refer to the following different satellite remote sensing channels: (grey dashed lines) six AIRS channels for dust retrieval in the thermal infrared (8.10, 8.15, 9.31, 10.36, 11.48, 11.86 µm); (black dashed line) IASI channel for dust optical depth retrieval at 10 µm; (grey shaded areas) the two MODIS broadband channels (10.78-11.28 and 11.77-12.27 µm) used for Sea Surface Temperature (SST) estimation.